Investigation of flow boiling in large micro-channel heat exchangers in a refrigeration loop for space applications

CrossMark

Seunghyun Lee, Issam Mudawar *

Boiling and Two-Phase Flow Laboratory (PU-BTPFL), School of Mechanical Engineering, Purdue University, 585 Purdue Mall, West Lafayette, IN 47907, USA

ABSTRACT

Future manned space endeavors will require a new class of vehicles, capable of conducting different types of missions and enduring varying gravitational and temperature environments. Thermal management will play a vital role in these new vehicles, and is complicated by the need to tackle both low and high heat sink temperatures. The present study concerns the development of a thermal management system operating in vapor compression mode to tackle high heat sink temperatures. The specific goal of the study is to investigate the two-phase heat transfer characteristics of two large micro-channel heat exchangers that serve as evaporators in the vapor compression loop using R134a as refrigerant. Both heat exchangers feature parallel micro-channels with identical 1×1-mm^2 cross-sections. The evaporators are connected in series, with the smaller 152.4-mm long heat exchanger situated upstream of the larger 609.6-mm long heat exchanger. This layout, along with broad ranges of mass velocity (152.90–530.72 kg/m^2 s) and base heat flux (8072.93–48,437.60 W/m^2) produced a wide range of qualities, which facilitated systematic assessment of dominant heat transfer mechanisms using both heat transfer measurements and high-speed video. Overall, it is shown low qualities are associated with slug flow and dominated by nucleate boiling, and high qualities with annular flow and convective boiling. Important transition points between the different heat transfer regimes are identified as (1) intermittent dryout, resulting from vapor blanket formation in liquid slugs and/or partial dryout in the liquid film surrounding elongated bubbles, (2) incipient dryout, resulting from dry patch formation in the annular film, and (3) complete dryout, following which the wall has to rely entirely on the mild cooling provided by droplets deposited from the vapor core. Finally, the study provides an assessment of the accuracy of eight previous correlations in predicting the measured two-phase heat transfer coefficient for both evaporators. Only one correlation is found to provide acceptable predictions in both accuracy and trend, evidenced by a mean absolute error of 21.19%, with 69.92% and 95.12% of the predictions falling within ±30% and ±50% of the data, respectively.

© 2016 Elsevier Ltd. All rights reserved.

1. Introduction

1.1. Thermal Control System (TCS) for future space missions

Increased scope, complexity and duration of future space missions are expected to increase both power consumption and rate of waste heat rejection from future space vehicles, which will have a profound adverse impact on the vehicle's size and weight [1]. Additionally, future space endeavors will require a new class of vehicles, capable of conducting different types of missions and enduring varying gravitational and temperature environments. These include missions to near Earth objects, Lunar surface, Martian surface, and deep space, as well as Lunar and Martian habitats.

One method for decreasing a space vehicle's size and weight is to replace current single-phase Thermal Control Systems (TCSs) with two-phase counterparts. The TCS maintains acceptable temperature and humidity levels for both crew and avionics, and consists of components that tackle heat acquisition, transport, and rejection. The size and weight reductions are achieved by capitalizing upon the latent heat of the working fluid, through evaporation and condensation, rather on sensible heat alone. With a two-phase TCS, the heat is acquired via evaporators and rejected by radiation via a condenser/radiator. The evaporators acquire heat from two main sources, crew and avionics, with a total thermal load for space vehicles ranging from 1.0 to 6.25 kW, depending on space mission [2]. On the other hand, thermal loads for Lunar and Martian habitats are estimated at 50 and 25 kW [3], respectively.

* Corresponding author. Tel.: +1 (765) 494 5705; fax: +1 (765) 494 0539.
  E-mail address: mudawar@ecn.purdue.edu (I. Mudawar).
  URL: https://engineering.purdue.edu/BTPFL (I. Mudawar).

Nomenclature

A_{base}	total base area of heat sink		*Greek symbols*	
Co	confinement number		β	ratio of micro-channel depth to width, $\beta = H_{ch}/W_{ch}$
D_b	bubble departure diameter		η	fin efficiency
d_h	hydraulic diameter		ρ	density
G	mass velocity		σ	surface tension
g	gravitational acceleration		θ	percentage predicted within ±30%
h	enthalpy		ζ	percentage predicted within ±50%
H_{ch}	micro-channel height			
h_{fg}	latent heat of vaporization		*Subscripts*	
H_{tc}	distance between thermocouple and base of micro-channel		3	three-sided heating
			4	four-sided heating
h_{tp}	local two-phase heat transfer coefficient		*avionics*	avionics H/X
$\bar{h}_{tp}$	average heat transfer coefficient		*b*	base of micro-channel
k	thermal conductivity		*ch*	micro-channel
L	micro-channel length		*cor*	correlation
m	fin parameter		*crew*	crew H/X
$\dot{m}$	mass flow rate		*di*	dryout incipience
Nu	Nusselt number		*exp*	experimental
p	Pressure		*f*	liquid
Q	heat input		*fo*	liquid only
q''	heat flux based on total base area of heat sink		*g*	vapor
q_h''	heat flux based heated perimeter		*in*	micro-channel inlet
T	temperature		*out*	micro-channel outlet
t	time		*pred*	predicted
W_{ch}	micro-channel channel width		*s*	solid (copper)
W_w	half-width of copper sidewall separating micro-channels		*sat*	saturation
			tc	thermocouple
x_{di}	quality corresponding to dryout incipience		*tp*	two-phase flow
x_e	thermodynamic equilibrium quality		*w*	micro-channel wall
z	coordinate along micro-channel			

Aside from increased size and weight, future space vehicles must endure broad variations in heat sink temperature. Space missions include (1) 'cold' environments, where the temperature of the working fluid exceeds the heat sink temperature, and (2) 'warm' environments, where the temperature of the working fluid is lower than the heat sink temperature. Cold environments enable heat rejection from the condenser/radiator using a pumped two-phase loop, while warm environments require a vapor compression heat pump to reject the heat. Most space missions provide cold environments. Two exceptions with environments are Low Lunar Orbit (LLO) and Low Mars Orbit (LMO), with heat sink temperatures as high as 17 and 22 °C, respectively [2], which exceed the lowest coolant temperature in the evaporators of 5 °C.

In recent years, researchers at the Purdue University Boiling and Two-Phase Flow Laboratory (PU-BTPFL) have developed several options for design of two-phase thermal managements systems [4]. They include such schemes as pool boiling [5], falling liquid films [6–8], channel flow boiling [9], spray cooling [10,11], and mini/micro-channel cooling [12–15], as well as cooling systems combining jet impingement and mini/micro-channel cooling [16]. However, factors such as reduced gravity, and the need to reduce TCS weight and size, tackle heat loads from multiple heat sources, and enhance system efficiency largely favor the use of mini/micro-channel cooling for space vehicles.

Clearly, a space vehicle must be able to tackle both cold and warm environments. To achieve this goal, Singh and Hasan [17] proposed a reconfigurable TCS that uses a single working fluid. This TCS would operate as a mechanically pumped two-phase loop (or even single-phase loop at low thermal loads) for cold environments, and a heat pump for warm environments. Lee et al. [2]

recently explored the design and thermodynamic performance of this type of Hybrid Thermal Control System (H-TCS) that satisfies the diverse thermal requirements of different space missions, endure both cold and hot environments, reduce size and weight, and enhance thermodynamic performance. R134a was deemed the most suitable working fluid based on its ability to provide a balanced compromise between reducing flow rate and maintaining low system pressure, and a moderate coefficient of performance (COP), let alone its favorable environmental attributes. The present study will address the thermal performance of mini/micro-channel evaporators that are used in conjunction with the heat pump configuration of a H-TCS.

1.2. Two-phase heat transfer in single mini/micro-channels

Two-phase flow and heat transfer characteristics of mini/micro-channels have been investigated experimentally in both single tubes and parallel multi-channel arrangements. References [18–22] are recent examples of studies addressing the heat transfer characteristics of single circular tubes. Lin et al. [18] investigated the effect of heat flux on the heat transfer coefficient for R141b in a vertical 1-mm diameter, 500-mm long tube over a mass velocity range of 300–2000 kg/m^2 and heat fluxes from 18 to 72 kW/m^2. Heat transfer at lower thermodynamic equilibrium qualities of $x_e < 0.4$ for 59,000 W/m^2 and $x_e < 0.03$ for 18,000 W/m^2 was dominated by nucleate boiling over the entire range of heat fluxes tested, evidenced by the heat transfer coefficient increasing with increasing heat flux and decreasing quality. On the other hand, the heat transfer coefficient was virtually independent of quality for $0.3 < x_e < 0.7$ in the intermediate heat flux range of
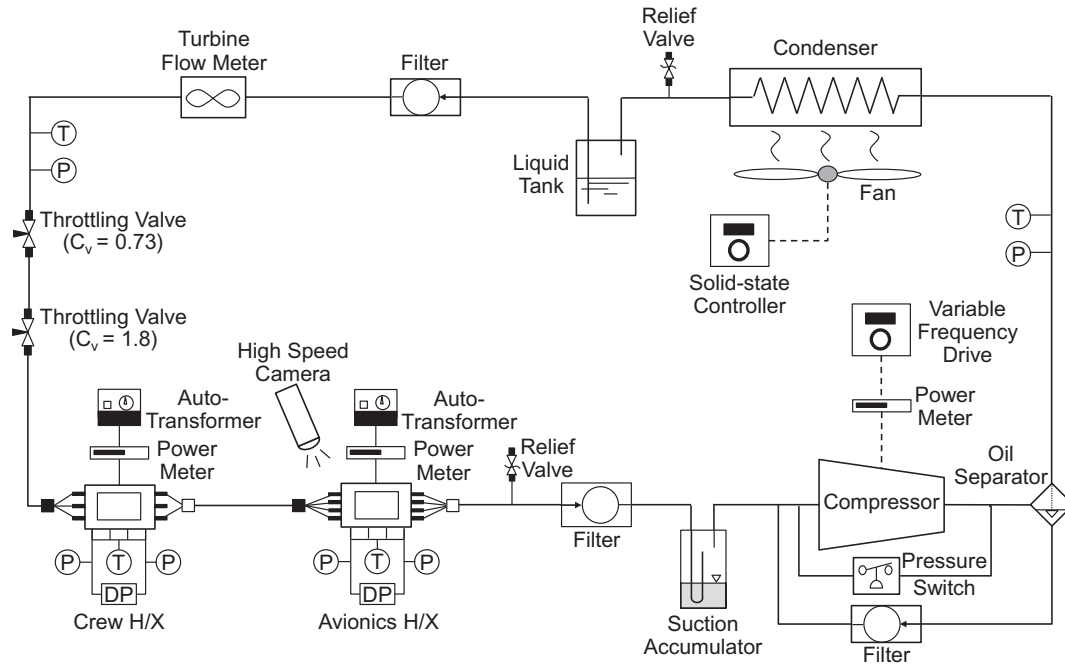
Fig. 1. Schematic diagram of vapor compression loop.

42,000–64,000 W/m^2. In and Jeong [19] measured different heat transfer coefficient trends for R123 and R134a in a 0.19-mm diameter, 31-mm long tube with a heated length of 20.6 mm. Nucleate boiling was dominant in the low quality region of $x_e < 0.6$ and convective boiling, where nucleate boiling is suppressed, in the high quality region of $0.6 < x_e < 0.85$ for R134a. Tibiriçá and Ribatski [20] measured the heat transfer characteristics for R134a and R245fa in a 2.3-mm diameter, 464-mm long tube. For mass velocities of R134a greater than 200 kg/m^2 s at 15 kW/m^2, the heat transfer coefficient was strongly dependent on heat flux and increased with increasing vapor quality for qualities as high as 0.9. Saisorn et al. [21] conducted flow boiling experiments with R134a in a 1.75-mm diameter, 600-mm long tube to relate heat transfer characteristics to dominant flow patterns for relatively high mass velocities of 200–1000 kg/m^2 s, and concluded that the local heat transfer coefficient increases with increasing heat flux but is independent of mass velocity or vapor quality as the flow pattern changes from slug to annular-rivulet. They also observed a degradation in heat transfer due to partial dryout in the annular-rivulet flow regime. Ducoulombier et al. [22] explored the effects of mass velocity, heat flux, and saturation temperature on the heat transfer coefficient for CO_2 in a 0.529-mm diameter, 191-mm long tube. They identified three heat transfer regimes: nucleate boiling, combined nucleate and convection boiling, and convective boiling. Overall, all these single-tube studies point to a gradual transition from nucleate boiling dominant to convective boiling dominant heat transfer with increasing quality.

1.3. Two-phase heat transfer in multi mini/micro-channels

Two-phase heat transfer characteristics of refrigerants in multi mini/micro-channels are typically conducted with the aid of a heat sink connecting a multitude of channels in parallel between constant pressure upstream and downstream plenums. Refrigerant multi-channel experiments have been conducted mostly using small heat sinks, which display heat transfer characteristics similar to those of single mini/micro-channels. In multi-channel studies, nucleate boiling is dominant at lower qualities, and encountered mostly in bubbly and slug flows, and convective boiling at higher qualities in annular flow.

Using a compact vapor compression loop, Lee and Mudawar [23] examined the two-phase flow and heat transfer characteristics of R134a using a 25.3 × 25.3-mm^2 copper heat sink containing 53 of 231 × 713-µm micro-channels and identified different heat transfer modes corresponding to different quality ranges. They also observed a decrease in the heat transfer coefficient in annular flow resulting from localized dryout. Agostini et al. [24] performed experiments with R236fa using a silicon heat sink containing 67 of 223 × 680-µm, 20-mm long micro-channels. By introducing the refrigerant in saturated state, they measured a decrease in the local heat transfer coefficient at high heat fluxes, which they attributed to intermittent dry-out.

Interestingly, different two-phase heat transfer trends have been observed in multi micro-channel experiments when using water as compared to refrigerants. In their water experiments, Qu and Mudawar [25,26] showed that convective boiling is dominant in micro-channels even at low qualities, which can be explained by the relatively large surface tension of water increasing bubble departure diameter, thereby suppressing nucleate boiling and triggering abrupt upstream transition to annular flow.

It is important to emphasize that the present study is focused on relatively large TCS evaporators containing a multitude of parallel, long micro-channels. Several prior studies have examined two-phase heat transfer for long single circular mini/micro-channels [18,20,21], but the findings from these studies cannot be confirmed for multi-channel evaporators. On the other hand, studies have been conducted with small multi mini/micro-channel heat sinks that are intended to manage high heat fluxes from very compact devices such as computer chips [18,23–27]. Despite their ability to tackle high heat fluxes, the corresponding total heat capacity of these heat sinks is comparatively small.

Large multi mini/micro-channels have been addressed in a small number of articles. They include a study by Kew and Cornwell [28], who identified four distinct heat transfer mechanisms similar to those they encountered later in single-tube studies [29]: nucleate boiling, confined bubble boiling, convective boiling,
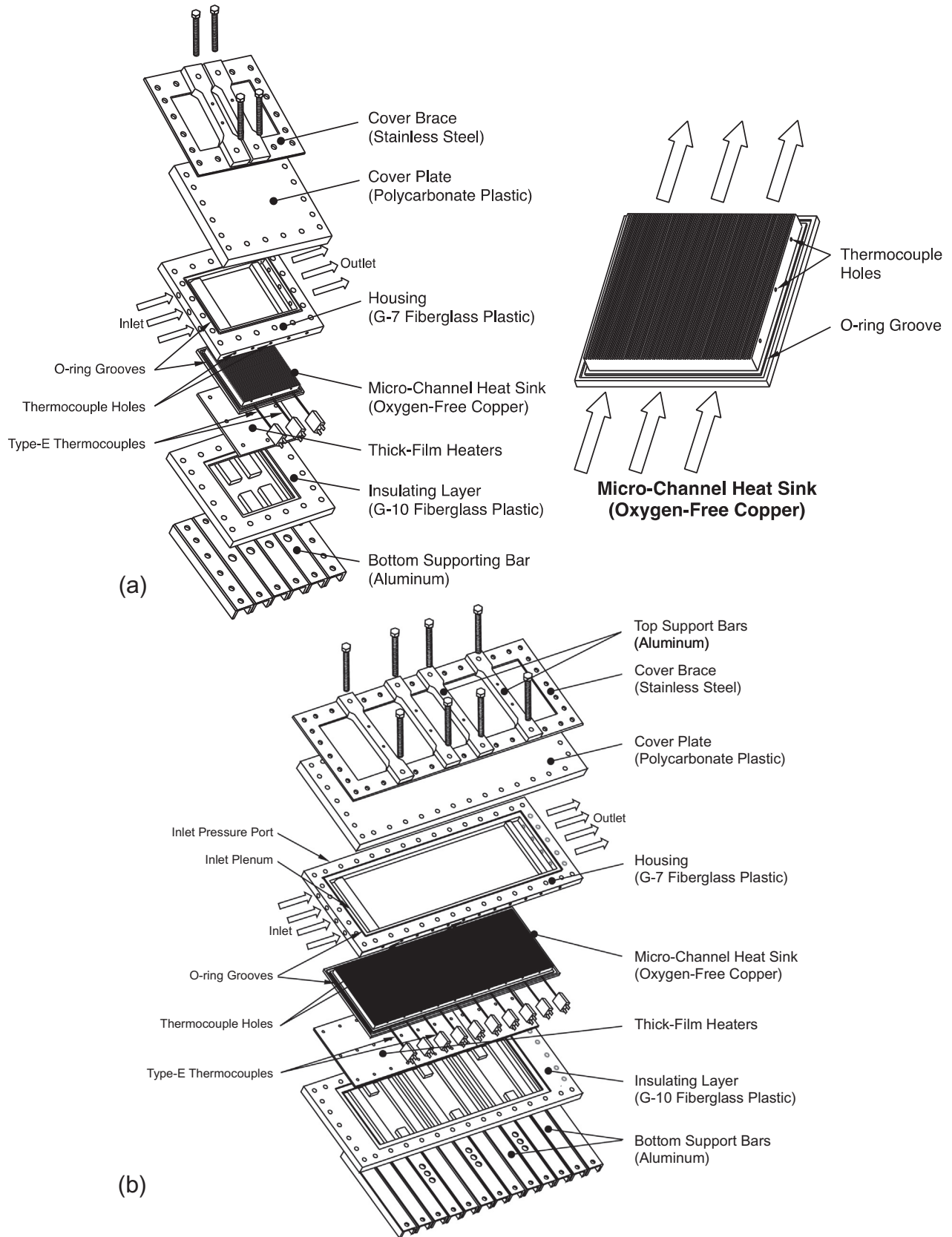
Fig. 2. Exploded views of (a) crew H/X and (b) avionics H/X.

Table 1
Crew and avionics micro-channel heat sink dimensions.

	Length [mm]	Width [mm]	Number of channels	Thermocouple axial locations [mm]
Crew H/X	152.4	152.4	75	22.9, 76.2, 129.5
Avionics H/X	609.6	203.2	100	44.2, 102.1, 160.0, 217.9, 275.8, 333.8, 391.7, 434.3, 507.5, 565.4

and partial dry-out. Jacobi and Thome proposed an alternative approach to predicting two-phase heat transfer behavior with their two-zone [30] and three-zone [31] models. They suggested the possibility that flow pattern can change periodically, but did not attempt to quantify the relationship between the measured heat transfer coefficient and cyclical flow patterns.

It is important to note that instabilities are inherent to many types of two-phase flows, and take the form of cyclical changes in flow patterns. Researchers have attempted to understand the causes and mechanisms of two-phase flow instabilities [32,33], including those specific to mini/micro-channels [34,35], and recommended practical means to dampening the more severe forms of instability or eliminating them altogether [34,36].

1.4. Objectives of study

The present study concerns the two-phase heat transfer characteristics of large micro-channel evaporators that are used in conjunction with the heat pump configuration of a H-TCS. First, heat transfer mechanisms will be related to dominant flow patterns that are captured with the aid of high-speed video. Next, the study will focus on heat transfer coefficient trends using a new large database, which is segregated based on quality range. Also discussed are the important phenomena of intermittent dryout for low quality and dryout incipience for high quality. Dryout plays a vital role in the implementation of a micro-evaporator in a refrigeration cycle, where high quality prevails over a significant portion of the channel length compared to small heat sinks. This study will also provide an assessment of prior predictive correlations for two-phase heat transfer coefficient against the newly measured data.

2. Experimental methods

2.1. Refrigeration loop

Fig. 1 shows a schematic diagram of the refrigeration loop that is designed to condition the working fluid to the desired inlet conditions to two micro-channel evaporators arranged in series: crew heat exchanger (H/X) and avionics H/X, which are sized to tackle the total heat rates associated with the crew and avionics, respectively, in a H-TCS system. R134a is selected as working fluid for the compression process based on its favorable thermodynamic performance [2]. This hydrofluorocarbon (HFC) also features zero Ozone Depletion Potential (ODP) and low Global Warming Potential (GWP). Heat is absorbed by the two evaporators via flow boiling, which increases quality to superheated vapor state. Superheating is necessitated by the loop's compressor, whose performance is compromised by any liquid entrained in the flow. Before entering the compressor, the superheated vapor is passed through a suction-side filter followed by a suction accumulator. The suction accumulator serves as a temporary reservoir, metering the ratio of oil flow rate in the refrigerant, and capturing any liquid to ensure only vapor flows into the compressor. The oil is necessary for lubrication of the compressor; polyolester oil is used in this study. A metering orifice is installed inside the suction accumulator to vaporize the liquid and protect the compressor from liquid

surge. Mixed with oil, the refrigerant vapor then enters the Copeland scroll compressor, where they are compressed together, then separated by an oil-separator. The scroll compressor is selected because of its low noise and vibration, and high coefficient of performance (COP). It also features high reliability because of its small number of moving parts compared to other compressor designs. The compressor's rotational speed is controlled by a variable frequency drive, which modulates the frequency of 200/230 VAC power input. Pressure switches are installed at the suction and discharge sides of the compressor to disconnect power input to the compressor should the pressure exceed or fall below prescribed limits. An oil separator downstream of the compressor uses centrifugal force to separate oil droplets from the refrigerant vapor. The oil accumulated on the bottom of the separator is returned to the suction side of the compressor where it is mixed with the refrigerant.

The hot compressed vapor flows to a Trenton air-cooled condenser, where it is converted to subcooled liquid by rejecting heat to ambient air. The speed of the condenser fan motor is regulated by a solid-state controller. The temperature of the subcooled liquid exiting the condenser can drop down to close to room temperature. The subcooled liquid is collected in a liquid reservoir and then passed through a liquid line filter, which is followed by a turbine flow meter for volumetric flow rate measurement. Throttling is achieved with the aid of two control valves in series, reducing pressure through isenthalpic expansion to the desired crew H/X's inlet value.

Humidity and moisture indicators are installed at several locations in the refrigeration loop for visual inspection of the flow state. The two-phase flow along the micro-channel evaporators is captured by a Photron-Ultima APX high-speed camera fitted with a 105-mm Nikkor lens. This camera is capable of shutter speeds up to 1/120,000 s.

2.2. Construction of micro-channel evaporators

Fig. 2(a) and (b) provide exploded diagrams illustrating the detailed constructions of the crew H/X and avionics H/X, respectively. These heat exchangers are identical in overall construction and micro-channel cross-section, but feature different numbers of micro-channels and different overall dimensions, as indicated in Table 1. The main component of each heat exchanger is the heat sink, made from oxygen-free copper, atop which the micro-channels are machined. The heat sink is heated uniformly along its underside by a Watlow thick film heater. The micro-channels are closed atop with a transparent cover plate made from polycarbonate plastic (Lexan), which provides optical access to the two-phase flow in the micro-channels. Two types of fiberglass plastic are used for thermal insulation. The first, G-7, is used to form a housing surrounding the copper heat sink, while G-10 is used to minimize heat loss from the perimeter and underside of the thick-film heater. Each evaporator is reinforced atop and below with metal braces to ensure tight assembly and minimize buckling of the intermediate layers. Fig. 3(a) shows a cross-section of the avionics H/X, which features 100 micro-channels; the smaller crew HX has similar construction but with smaller overall dimensions and only 75 micro-channels.
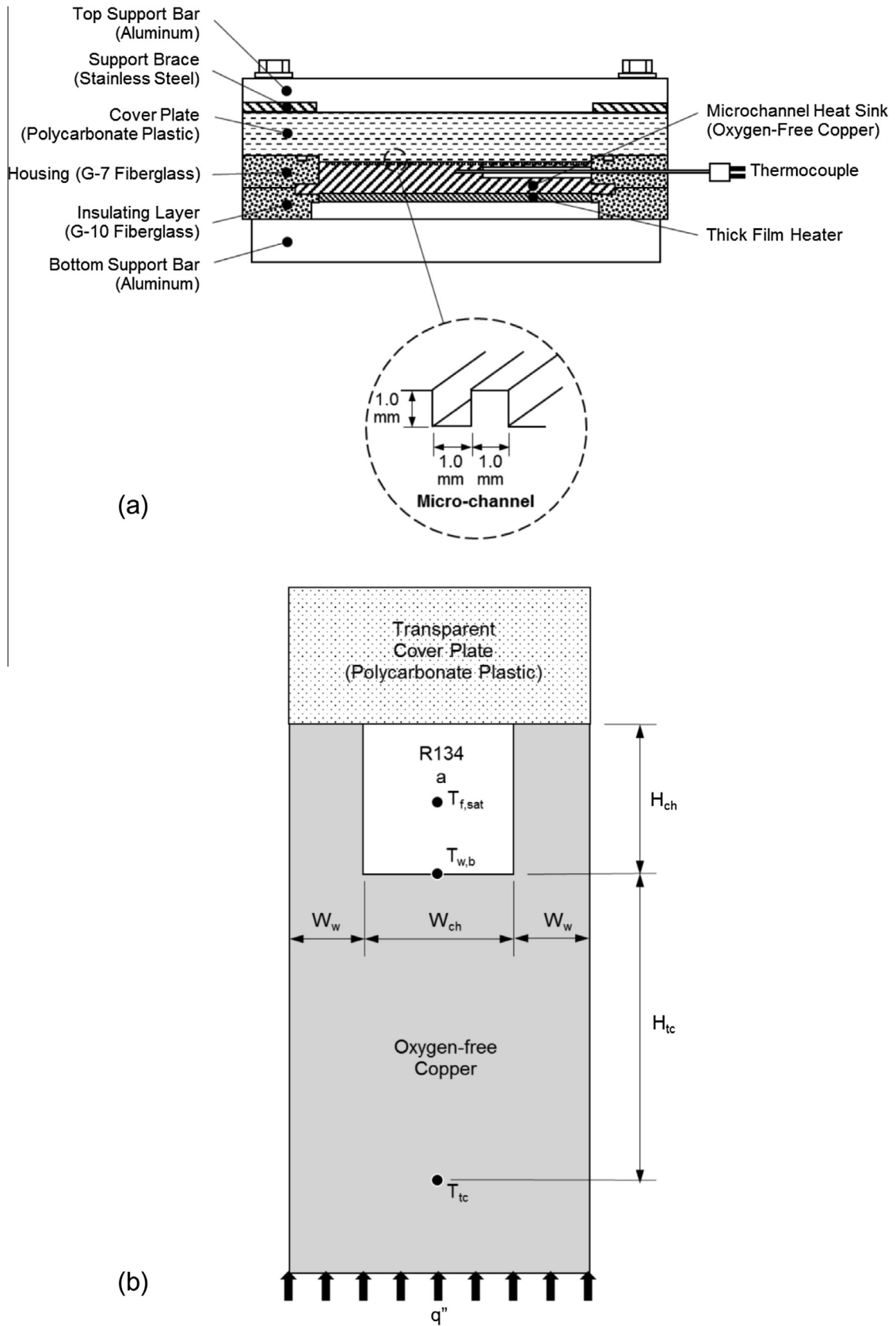
(a)

(b)

Fig. 3. (a) Cross-sectional view of avionics H/X. (b) Two-dimensional micro-channel heat sink unit cell in both crew H/X and avionics H/X.

Table 2
Measurement error and uncertainty propagation.

Parameter	Error (%)	Parameter	Uncertainty (%)
Absolute pressure	±0.1	Heat transfer coefficient, h_{tp}	⩽5.92
Differential pressure	±0.1	Pressure drop, Δp	⩽0.1
Temperature, T	±0.5	Vapor quality change, Δx_e	⩽3.23
Mass flow rate, $\dot{m}$	±0.12		
Heat input, Q	±0.3		

Table 3
Operating conditions for crew H/X and avionics H/X.

$q''_{avionics}$ [W/m²]	$G_{avionics}$ [kg/m² s]	$x_{e,in}$	$x_{e,out}$	Number of h_{tp} data points (1000 total)
Avionics H/X				
8072.9	152.90–225.97	0.1850–0.2377	0.4071–0.5586	50
12,109.4	155.27–266.84	0.1641–0.2324	0.4496–0.6995	70
16,145.9	154.66–286.18	0.1475–0.2367	0.5060–0.8599	80
20,182.3	154.45–322.53	0.1389–0.2269	0.5464–1.2233	100
24,218.8	153.70–359.93	0.1108–0.2332	0.5533–1.4369	120
28,255.3	152.83–361.70	0.1052–0.2274	0.6211–1.5677	120
32,291.7	172.31–381.24	0.0868–0.2121	0.6546–1.5369	120
36,328.2	193.07–398.55	0.0891–0.1892	0.6941–1.4988	120
40,364.7	232.60–416.25	0.0852–0.1654	0.7450–1.3366	110
44,401.1	249.63–434.31	0.0703–0.1511	0.7671–1.3598	110

q''_{crew} [W/m²]	G_{crew} [kg/m² s]	$x_{e,in}$	$x_{e,out}$	Number of h_{tp} data points (144 total)
Crew H/X				
8072.9	229.33–529.63	0.0729–0.1974	0.1191–0.2715	24
16,145.9	230.59–527.18	0.0765–0.1951	0.1528–0.3250	24
24,218.8	229.30–528.50	0.0700–0.1922	0.1744–0.3825	24
32,291.7	230.94–532.27	0.0515–0.1785	0.1823–0.4253	24
40,364.7	229.00–526.96	0.0626–0.1787	0.2278–0.4883	24
48,437.6	233.34–530.72	0.0535–0.1627	0.2448–0.5298	24

Table 4
Dimensions of micro-channel heat sink unit cell in both crew H/X and avionics H/X.

W_w [mm]	W_{ch} [mm]	H_{ch} [mm]	H_{tc} [mm]
0.5	1.0	1.0	4.08

The evaporators feature multiple inlet and outlet flow ports, three for crew HX and four for the avionics HX, which help enhance flow uniformity among the micro-channels. Equal flow distribution between inlet ports is provided by a Sporlan Venturi throat distributor.

2.3. Measurement instrumentation and data acquisition

As shown in Fig. 2(a) and (b), the copper heat sink temperature is measured at several axial locations with the aid of Type-E thermocouples, which possess the highest Seebeck coefficient of 68 μV/°C among the different thermocouple types. Each thermocouple is inserted along a stainless steel sheath, with the junction reaching the centerline of the copper heat sink.

Pressure is measured at the inlet and outlet in each evaporator by a combination of an Omega-MMA absolute pressure transducer and a Honeywell-THE differential pressure transducer. Also installed at the inlet and outlet of each evaporator are glycerin-filled pressure gauges that are used to make certain that the transducers are in proper working order.

Volumetric flow rate is measured by a Flow Technology turbine flow meter, which is installed in the single-phase liquid region of the refrigeration loop.

A three-phase power meter measures the true power (W) of the compressor, which is different from the apparent power because the current and voltage are out of phase due to the compressor's reactance. A Yokogawa power meter is used to measure the voltage, current, and power input to the thick film heaters from an autotransformer. An FET multiplexer collects signal from the thermocouples, pressure transducers, flow meter, and power meter, which are processed by an HP data acquisition system. The measurement errors and uncertainty propagated in the calculated parameters are provided in Table 2, where the uncertainty is determined by the root sum square method [37,38].

2.4. Operating conditions

Throttling valves situated between the turbine flow meter and the crew H/X are used to decrease liquid pressure to the crew H/X's inlet pressure, causing the liquid to flash into a two-phase mixture. The enthalpy value at the inlet to the crew H/X is equal to that determined from the pressure and temperature of liquid at the inlet to the throttling valves, assuming isenthalpic pressure drop across the valves. The vapor quality at the inlet to the crew H/X is determined from the measured pressure at the crew H/X's inlet and the inlet enthalpy, h.

$$x_{e,in} = \frac{h - h_f}{h_{fg}}, \tag{1}$$

where h_f and h_{fg} are saturated values based on the crew H/X's inlet pressure. The crew H/X's outlet quality is determined by applying an energy balance to the entire crew H/X,
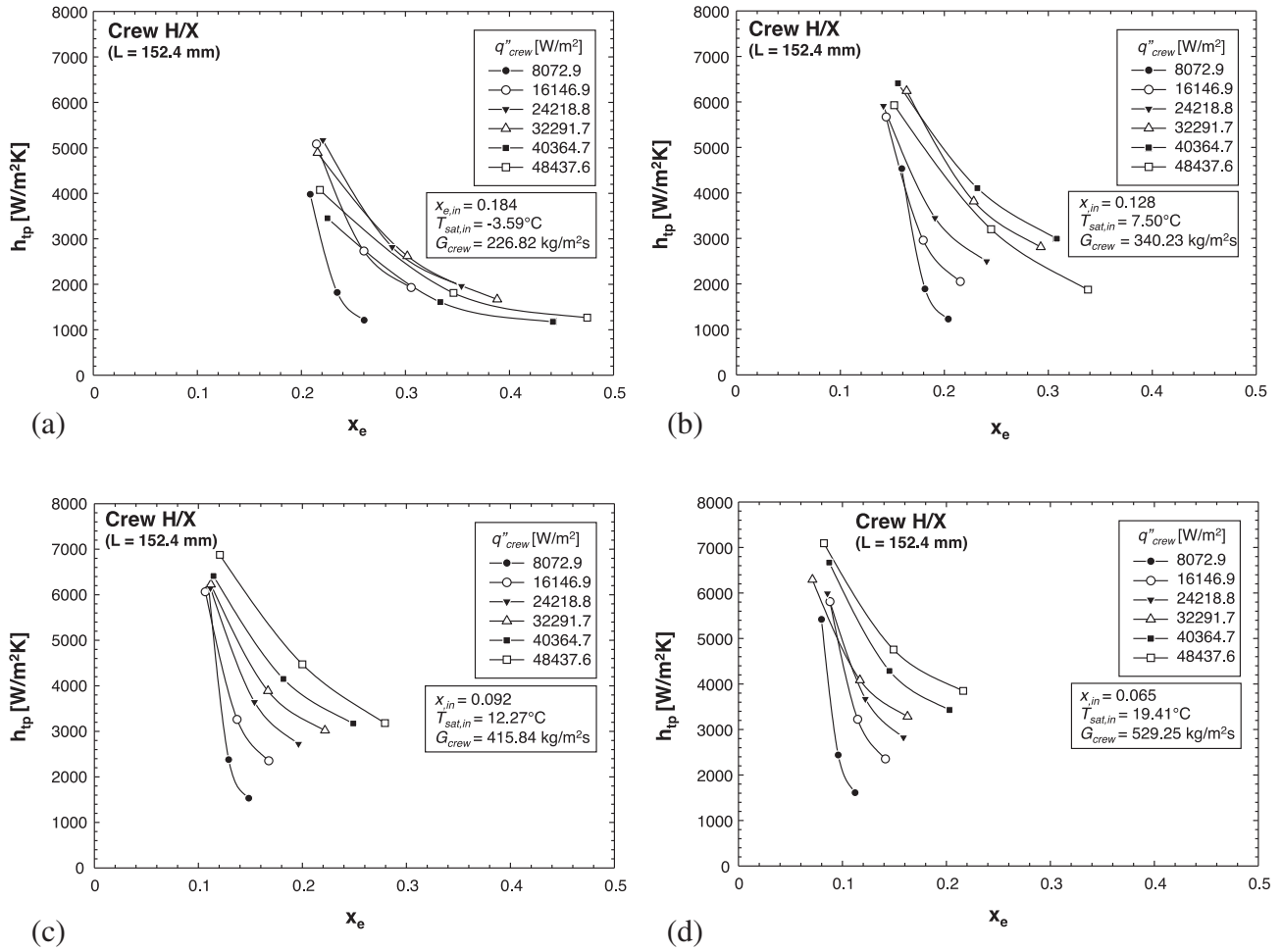
Fig. 4. Crew HX's variation of two-phase heat transfer coefficient with thermodynamic equilibrium quality for different heat fluxes and (a) G_{crew} = 226.82 kg/m² s, (b) G_{crew} = 340.23 kg/m² s, (c) G_{crew} = 415.84 kg/m² s, and (d) G_{crew} = 529.25 kg/m² s.

$$x_{e,out} - x_{e,in} = \frac{q'' A_{base}}{\dot{m} h_{fg}}, \qquad (2)$$

where q'' is the heat flux based on the heat sink's bottom area, A_{base}, and $\dot{m}$ is the total flow rate of R134a. Table 3 provides the operating conditions for the present study. The mass flow rate is adjusted to yield a relatively high quality at the outlet of the avionics H/X in excess of 0.4 to ensure proper compressor operation.

3. Determination of heat transfer coefficient

Fig. 3(b) shows a unit control volume consisting of a single micro-channel and half of the surrounding copper walls; the detailed dimensions of the unit cell are provided in Table 4. A simplified fin model is applied to the copper walls in order to construct an energy balance for the unit cell. The two-phase heat transfer coefficient, h_{tp}, is determined by equating the heat input from the underside of the copper heat sink to convection along the micro-channel walls, with the sidewalls treated as fins,

$$h_{tp} = \frac{q''(W_{ch} + 2W_w)}{(T_{w,b} - T_{f,sat})(W_{ch} + 2\eta H_{ch})}, \qquad (3)$$

where η is the efficiency for a fin with an adiabatic tip [39],

$$\eta = \frac{\tanh(m H_{ch})}{m H_{ch}}, \qquad (4)$$

and m the fin parameter,

$$m = \sqrt{\frac{h_{tp}}{k_s W_w}}. \qquad (5)$$

The micro-channel's bottom wall temperature, $T_{w,b}$, is calculated by assuming one-dimensional heat conduction between the planes of the thermocouple and bottom wall,

$$T_{w,b} = T_{tc} - \frac{q'' H_{tc}}{k_s}. \qquad (6)$$

The fluid saturation temperature, $T_{f,sat}$, along the micro-channel is determined from the corresponding saturation pressure, with the latter calculated by assuming a linear pressure drop from the inlet to the outlet.

4. Experimental results

4.1. Quality differences for crew H/X versus avionics H/X

An important objective in the present study is to identify conditions for which heat transfer is dominated by nucleate boiling as opposed to convective boiling. It should be emphasized that, because of different heat capacities and relative locations in the refrigeration loop, the heat exchangers are associated with different quality ranges. With a 152.4-mm length and maximum heat input of 1125 W, the crew H/X is associated with relatively low
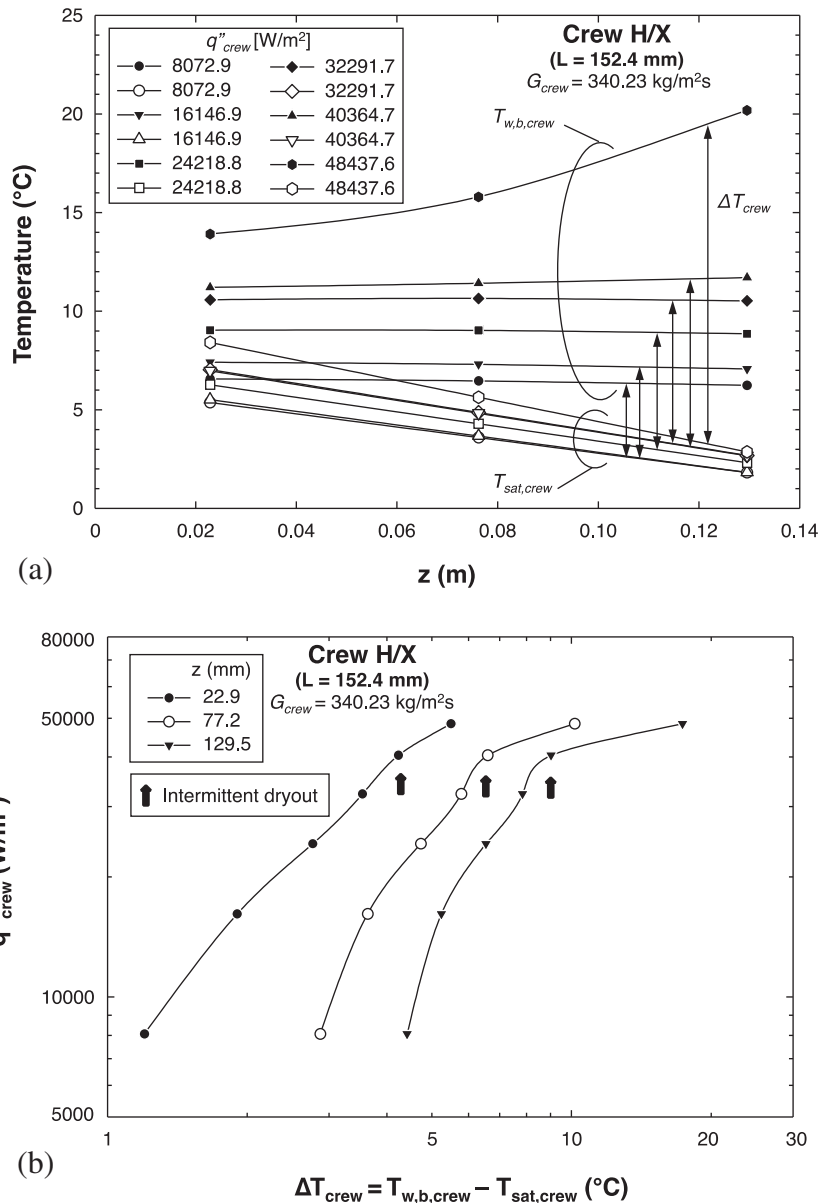
Fig. 5. (a) Axial variations of bottom channel wall temperature, $T_{w,b,crew}$, and saturation temperature, $T_{sat,crew}$, along crew H/X for different heat fluxes and G_{crew} = 340.23 kg/ m² s. (b) Variation of crew H/X's boiling curve along the flow direction for G_{crew} = 340.23 kg/m² s.

quality values. On the other hand, the 609.6-mm length and maximum heat input of 5500 W allow the avionics H/X to achieve both low and high quality values. Low quality values in the avionics H/X are achieved by setting heat input to the upstream crew H/X to zero.

4.2. Influence of heat flux

4.2.1. Heat flux trends for crew H/X (low x_e range)

Fig. 4(a)–(d) show, for the crew H/X, the variation of measured two-phase heat transfer coefficient, h_{tp}, with thermodynamic equilibrium quality, x_e, for different heat fluxes and G_{crew} = 226.82, 340.23, 415.84, and 529.25 kg/m² s, respectively. Notice that quality values for the crew H/X are relatively low, below 0.5. Additionally, inlet quality decreases from x_e = 0.184 to 0.0645 and inlet temperature increases from −3.59 to 19.41 °C as mass velocity is increased from G_{crew} = 226.82 to 529.25 kg/m² s. This trend in inlet conditions, which is evident from a temperature-entropy diagram,

is the result of a decrease in the throttling pressure drop with increasing G_{crew}, which increases the crew H/X's inlet pressure, and therefore inlet temperature while preserving the enthalpy upstream of the throttling valves.

Fig. 4(a)–(d) show the heat transfer coefficient, h_{tp}, generally increases with increasing heat flux, q''_{crew}, and decreasing quality, x_e, for fixed mass velocity, G_{crew}, which is indicative of heat transfer dominated by nucleate boiling. Because h_{tp} decreases with increasing x_e, convective boiling appears to be a minor contributor to heat transfer. This suggests that annular flow is not well established. However, Fig. 4(a), which is associated with the highest x_e values for the crew H/X, does show a tendency for h_{tp} to become fairly insensitive to q''_{crew} and x_e for x_e > 0.3. This trend points to a transition from nucleate boiling dominant to convective boiling dominant behavior for this specific higher x_e range.

Fig. 5(a) shows, for G_{crew} = 340.23 kg/m² s, axial variations of the micro-channel's saturation temperature, $T_{sat,crew}$, and bottom wall temperature, $T_{w,b,crew}$, along the crew H/X for different heat fluxes.
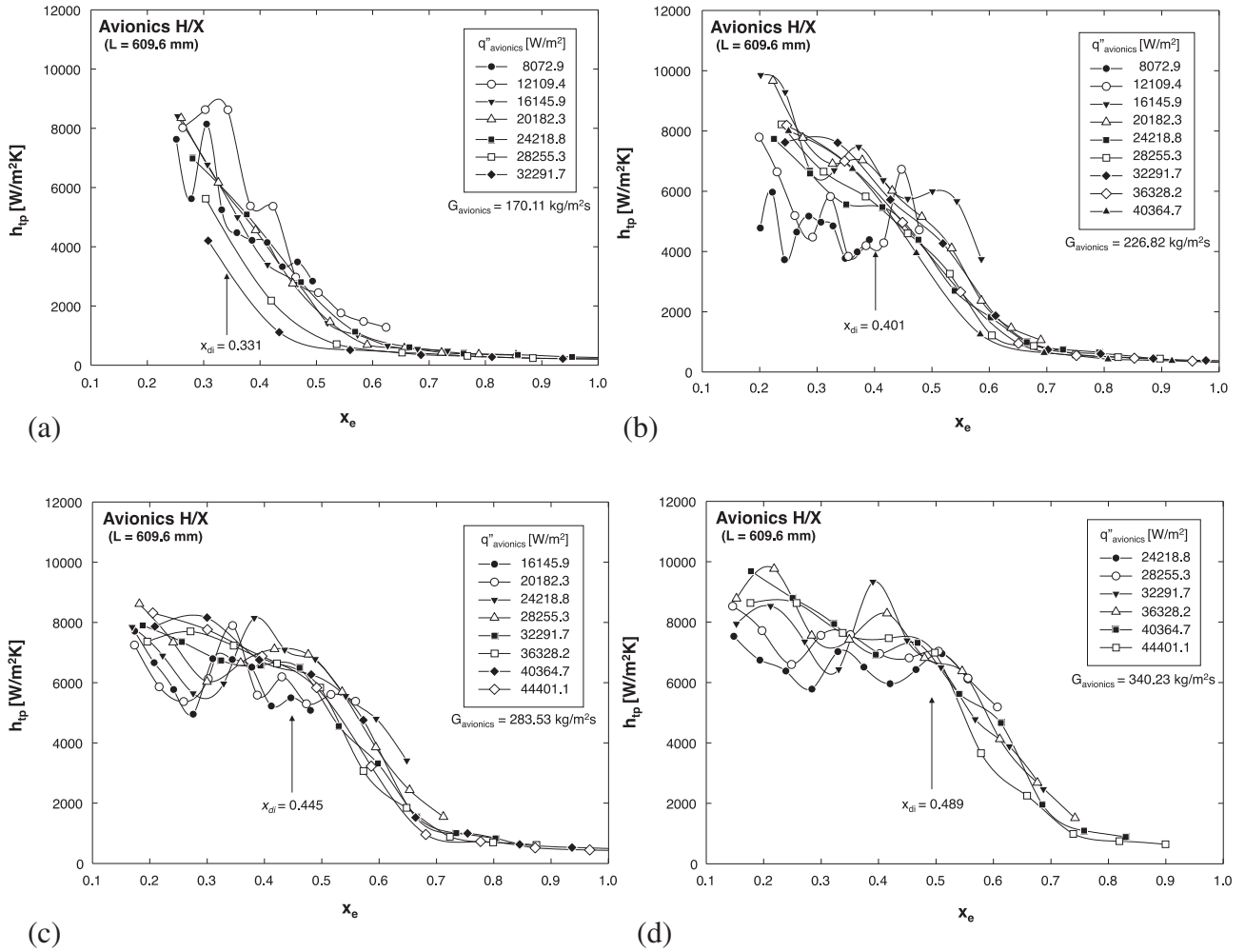
Fig. 6. Avionics HX's variation of two-phase heat transfer coefficient with thermodynamic equilibrium quality for different heat fluxes and (a) $G_{avionics}$ = 170.11 kg/m^2 s, (b) $G_{avionics}$ = 226.82 kg/m^2 s, (c) $G_{avionics}$ = 283.53 kg/m^2 s, and (d) $G_{avionics}$ = 340.23 kg/m^2 s.

$T_{sat,crew}$ is shown decreasing monotonically along the micro-channel because of the decreasing pressure. However, excluding the highest heat flux of q''_{crew} = 48,437.6 W/m^2, the axial variation in $T_{w,b,crew}$ is much smaller, and increasing q''_{crew} has a stronger influence on $T_{w,b,crew}$ than on $T_{sat,crew}$. Most noticeable is the appreciable increase in ΔT_{crew} (=$T_{w,b,crew} - T_{sat,crew}$) as q''_{crew} is increased from 40,364.7 to 48,437.6 W/m^2. This increase is primarily the result of a significant increase in $T_{w,b,crew}$ towards the downstream region of the crew H/X. Since these events occur in a nucleate boiling dominant region, they suggest heat transfer degradation is due to *intermittent dryout* before the formation of a continuous thin annular film. Intermittent dryout during nucleate boiling, which occurs prior to CHF, can be explained by a combination of coalescence of bubbles triggering intermittent formation of localized insulating vapor blankets and/or dryout in the liquid film surrounding an elongated bubble in slug flow. This phenomenon is clearly reflected in Fig. 4(b) in the form of a reversal in the trend of h_{tp} versus q''_{crew} at q''_{crew} = 40,364.7 W/m^2.

This trend is further illustrated in the boiling curves for the crew H/X, Fig. 5(b), corresponding to the same G_{crew} = 340.23 kg/m^2 s at three axial locations. Notice the large degradation in boiling performance with increasing z as q''_{crew} is increased from 40,364.7 to 48,437.6 W/m^2. It can be concluded that the large change in slope at q'' = 40,364.7 W/m^2, where h_{tp} reaches maximum value for G_{crew} = 340.23 kg/m^2 s, is the result of localized intermittent dryout.

4.2.2. Heat flux trends for avionics H/X (low to high x_e range)

Fig. 6(a)–(d) show, for the avionics H/X, the variation of the measured two-phase heat transfer coefficient, h_{tp}, with thermodynamic equilibrium quality, x_e, for different heat fluxes and $G_{avionics}$ = 170.11, 226.82, 283.58, and 340.23 kg/m^2 s, respectively. As indicated earlier, being much longer than the crew H/X, the avionics H/X provides a much broader x_e range that includes both small and large values. There is a sharp decrease in h_{tp} at a specific x_e value that depends on $G_{avionics}$. The effect of $q''_{avionics}$ is quite small above this x_e value, indicating nucleate boiling is suppressed in the high x_e range. On the other hand, h_{tp} exhibits appreciable sensitivity to $q''_{avionics}$ in the lower x_e range. Notice that the sharp decrease in h_{tp} occurs at x_e values much larger than those associated with the crew H/X. And unlike the nucleate boiling regime for most crew H/X operating conditions, the higher x_e values for the avionics H/X are representative of annular flow and dominated by convective boiling. It can therefore be concluded that the heat transfer degradation in the avionics H/X is the results of *dryout incipience*, or localized dryout of the annular liquid film, rather than the aforementioned intermittent dryout.

In this study, dryout incipience is loosely identified for each heat flux by the x_e value where h_{tp} decreases by 30% from its inlet value, and the dryout incipience values for all heat fluxes are then averaged to yield a single value, x_{di}, for a given mass velocity. Fig. 6(a)–(d) show x_{di} generally increases with increasing mass velocity, from 0.331 at 170.11 kg/m^2 s to 0.489 at 340.23 kg/m^2 s. This trend
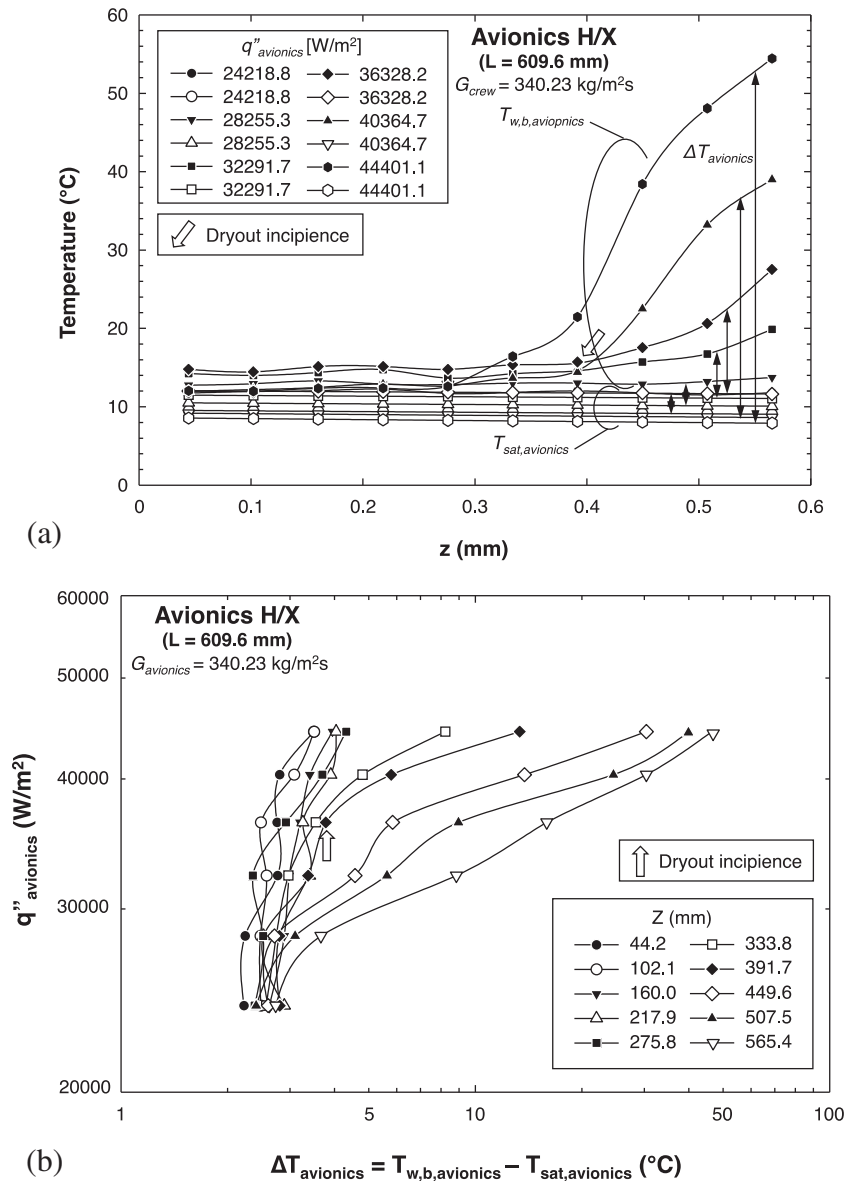
Fig. 7. (a) Axial variations of bottom channel wall temperature, $T_{w,b,avionics}$, and saturation temperature, $T_{sat,avionics}$, along avionics H/X for different heat fluxes and $G_{avionics}$ = 340.23 kg/m² s. (b) Variation of avionics H/X's boiling curve along the flow direction for $G_{avionics}$ = 340.23 kg/m² s.

is consistent with that of a recently published dryout incipience correlation for relatively low heat fluxes [40].

Fig. 7(a) shows saturation temperature is fairly constant along the avionics H/X. Additionally, the wall temperature shows only mild sensitivity to heat flux along the micro-channel upstream, but increases appreciably downstream from the dryout incipience point, which corresponds to z = 391.7 mm and $q''_{avionics}$ = 36,328.2 W/m². This point is also indicated in the boiling curve for the same mass velocity, Fig. 7(b), corresponding to the third highest heat flux in Fig. 6(d). Fig. 7(a) and (b) show the wall temperature beginning to increase rapidly at the dryout incipience point.

Previous micro-channel refrigerant boiling experiments have shown heat transfer to be dominated by nucleate boiling in the bubbly and slug flow regimes and convective boiling in the annular flow regime [23,41]. The transition between the two boiling mechanisms has been attributed to suppression of bubble nucleation by thin-film evaporation in the annular flow regime. This transition is

also influenced by the mass flow rate and momentum of the annular liquid film, and by shear stress between the vapor core and liquid film.

Using Fig. 6(d) as example, nucleate boiling is suppressed around x_e = 0.3, below which h_{tp} increases with increasing heat flux. Intermittent dryout is observed for x_e < 0.3 for the higher heat flux, q''_{crew} = 40,364.7 W/m², and h_{tp} decreases monotonically in the absence of a convective boiling regime where the heat transfer coefficient increases with vapor quality. Above x_e = 0.3, convective boiling becomes dominant, increasing h_{tp} with increasing x_e until the dryout incipience point, x_{di} = 0.489. Qualities above this value cause further liquid film dryout, with the cooling sustained in part by deposition of droplets entrained in the vapor core. It is suggested h_{tp} decreases with increasing x_e for $x_e > x_{di}$ because of a gradual decline in the number and rate of deposited droplets [42]. Farther downstream, a predominantly vapor flow region is established as x_e approaches unity, and the transfer coefficient decreases to a low value with little sensitivity to x_e.
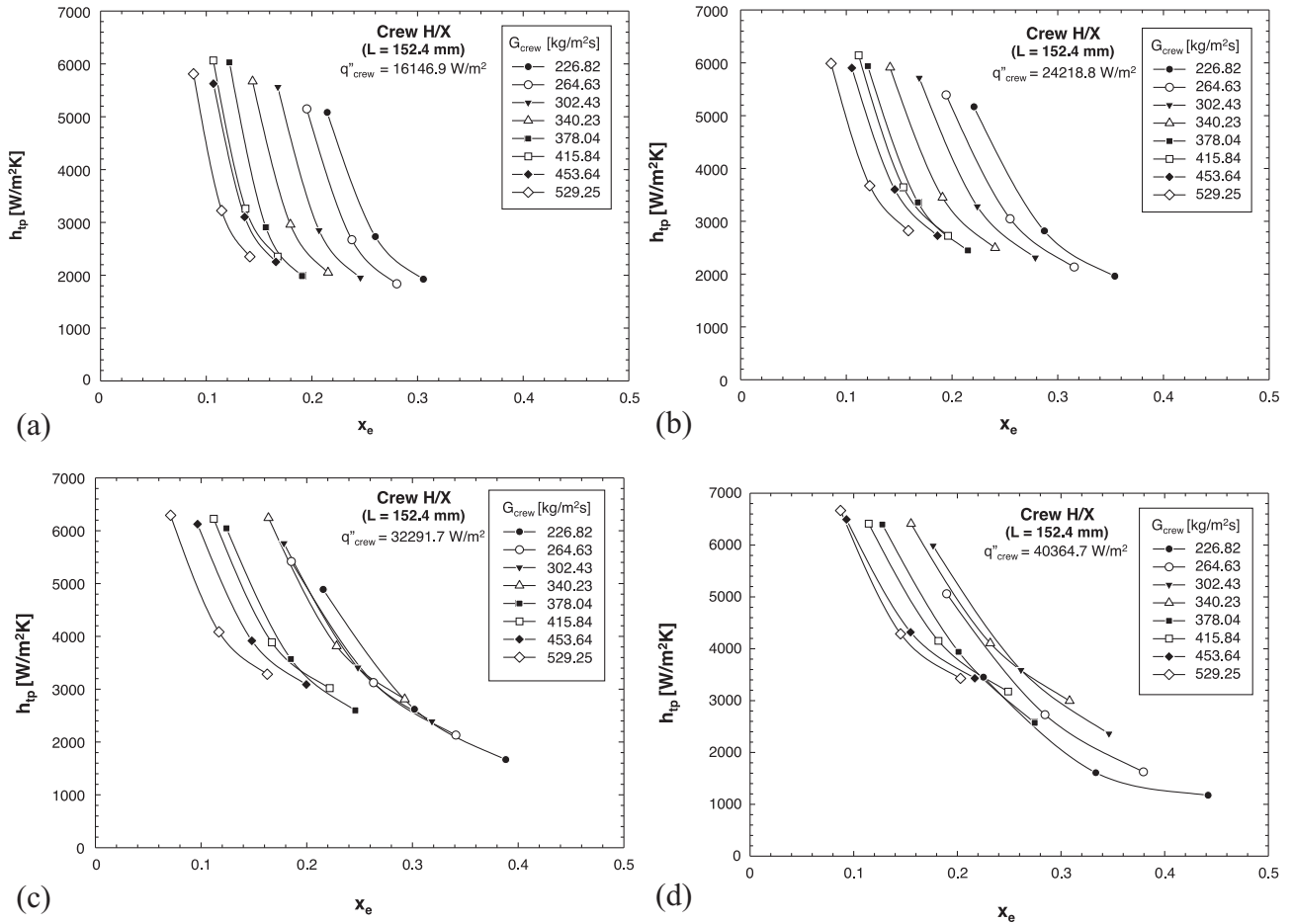
Fig. 8. Crew HX's variation of two-phase heat transfer coefficient with thermodynamic equilibrium quality for different mass velocities and (a) q''_{crew} = 16,146.9 W/m², (b) q''_{crew} = 24,218.8 W/m², (c) q''_{crew} = 32,291.7 W/m², and (d) q''_{crew} = 40,364.7 W/m².

4.3. Influence of mass velocity

4.3.1. Mass velocity trends for crew H/X (low x_e range)

Fig. 8(a)–(d) show, for the crew H/X, variations of the two-phase heat transfer coefficient, h_{tp}, with quality, x_e, for different mass velocities and q''_{crew} = 16,146.9, 24,218.8, 32,291.7 and 40,364.7 W/m², respectively. Notice that inlet quality increases with decreasing G_{crew} because of the increased throttling as discussed earlier. For each combination of q''_{crew} and G_{crew}, these figures show h_{tp} decreases sharply for low x_e values but more mildly with increasing x_e. The combination of highest q''_{crew} of 40,364.7 W/m² and lowest G_{crew} of 226.82 kg/m² s, Fig. 8(d), is shown yielding the highest exit x_e value, where the decrease in h_{tp} with increasing x_e is most subdued.

4.3.2. Mass velocity trends for avionics H/X (low to high x_e range)

Fig. 9(a)–(d) show, for the avionics H/X, variations of the two-phase heat transfer coefficient, h_{tp}, with quality, x_e, for different mass velocities and q''_{crew} = 8072.9, 20,182.3, 32,291.7 and 44,401.1 W/m², respectively. As discussed earlier, h_{tp} for the avionics H/X shows an appreciable decrease with increasing x_e to a fairly constant downstream value. The lowest heat flux of q''_{crew} = 8072.9 W/m², Fig. 9(a), shows the lowest exit x_e values, especially for the highest mass velocity of $G_{avionics}$ = 226.82 kg/m² s. On the other hand, the highest three heat fluxes, Fig. 9(b)–(d), show exit x_e values approaching unity, especially for lower mass velocities.

5. Flow visualization results

5.1. Temporal fluctuations due to instabilities in mini/micro-channels

As discussed in [34,43], flow boiling in mini/micro-channels is fundamentally different from that in macro-channels, especially in a heat exchanger containing multiple channels. Most important among these differences are flow instabilities and bubble confinement effects.

Previous studies point to two main forms of flow instability in parallel mini/micro-channels: severe pressure drop oscillation and parallel channel instability [34]. The former is associated with highly periodic and high pressure oscillations, with identical flow patterns fluctuating in unison between the parallel mini/micro-channels. A simple and highly effective method to preventing the pressure drop oscillation is to throttle the flow, especially upstream of the micro-channel heat sink. The second form of instability is associated with short duration and small pressure oscillations that occur with less regularity among the parallel micro-channels. This milder form of instability can be reduced but not eliminated with upstream throttling. This is the type of instability encountered in the present study. It is important to note that a refrigeration cycle such as the one used in this study requires placing a throttling valve upstream of the evaporators, which provides the benefit of eliminating the severe pressure drop oscillation altogether.

Another phenomenon that is unique to mini/micro-channels is anisotropic bubble growth, where bubble growth across the flow
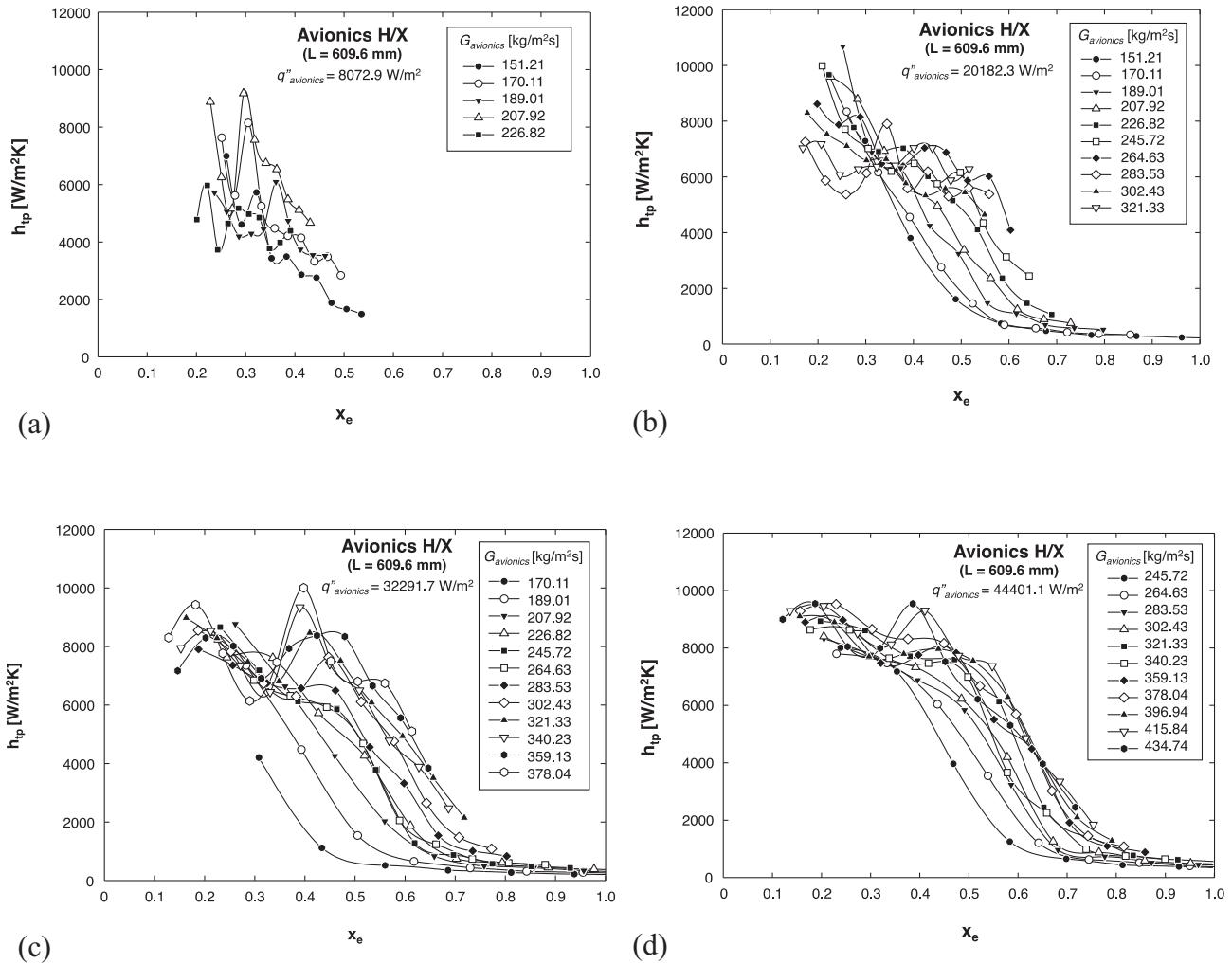
Fig. 9. Avionics HX's variation of two-phase heat transfer coefficient with thermodynamic equilibrium quality for different mass velocities and (a) $q''_{avionics}$ = 80,72.9 W/m², (b) $q''_{avionics}$ = 20,182.3 W/m², (c) $q''_{avionics}$ = 33,291.7 W/m², and (d) $q''_{avionics}$ = 44,401.1 W/m².

area is suppressed by the small diameter of the flow channel. Once nucleation is initiated, bubbles growth and/or coalescence in the radial direction occur very fast, and the only remaining direction for bubble growth is axially along the channel. This phenomenon causes the bubbly flow regime in mini/micro-channels to occur over only a short upstream portion of the channel length, and results in early transition from bubbly to slug flow compared to macro-channels. Kew and Cornwell [29] suggested relying on the *confinement number* to determine when mini/micro-channel confinement effects are dominant. The confinement number is the ratio of the bubble detachment diameter, D_b, to the channel's hydraulic diameter, d_h,

$$Co = \frac{D_b}{d_h}, \tag{7}$$

where

$$D_b = \sqrt{\frac{\sigma}{g(\rho_f - \rho_g)}}, \tag{8}$$

with $Co > 0.5$ indicating a strong tendency for bubble confinement.

5.2. Flow visualization results for crew H/X

A key advantage of high-speed video imaging that is not available from the heat transfer data is the ability to capture both dominant flow regimes and transient interfacial behavior. Fig. 10 shows flow behavior along the crew H/X for G_{crew} = 378.04 kg/m² s and q''_{crew} = 32,291.7 W/m² prior to intermittent dryout. The images shown match those of the heat transfer coefficient plot provided in Fig. 8(c), with quality values below x_e = 0.25. Eleven images are shown whose axial center corresponds to the middle of the crew H/X, z = 76.2 mm, and which capture cyclical events associated with flow pattern transitions over about a 60-ms period. This figure shows local temporal fluctuations in both mass velocity and quality are quite prevalent. While some of the images may seem representative of annular flow, they actually capture slug flow with long bubbles whose front and/or tail fall outside the image boundaries. Interestingly, the confinement number for the flow conditions in this figure is Co = 0.9246, which implies a clear confinement tendency and therefore early transition from the bubbly flow regime to the observed slug flow regime. The temporal fluctuations in flow rate are reflected in two distinct durations: a *liquid abundant duration* and a *liquid deficient duration*, each lasting 600–650 ms depending on operating conditions, and encompassing three to four of the aforementioned 60-ms cycles separated by waiting periods. As mass flow rate increases momentarily, the liquid abundant period is initiated with an elongated bubble with a thickening liquid film as shown at t = 0 ms, when the film begins to evaporate slowly. Shear forces exerted by the faster vapor core on the interface of the liquid film induces small
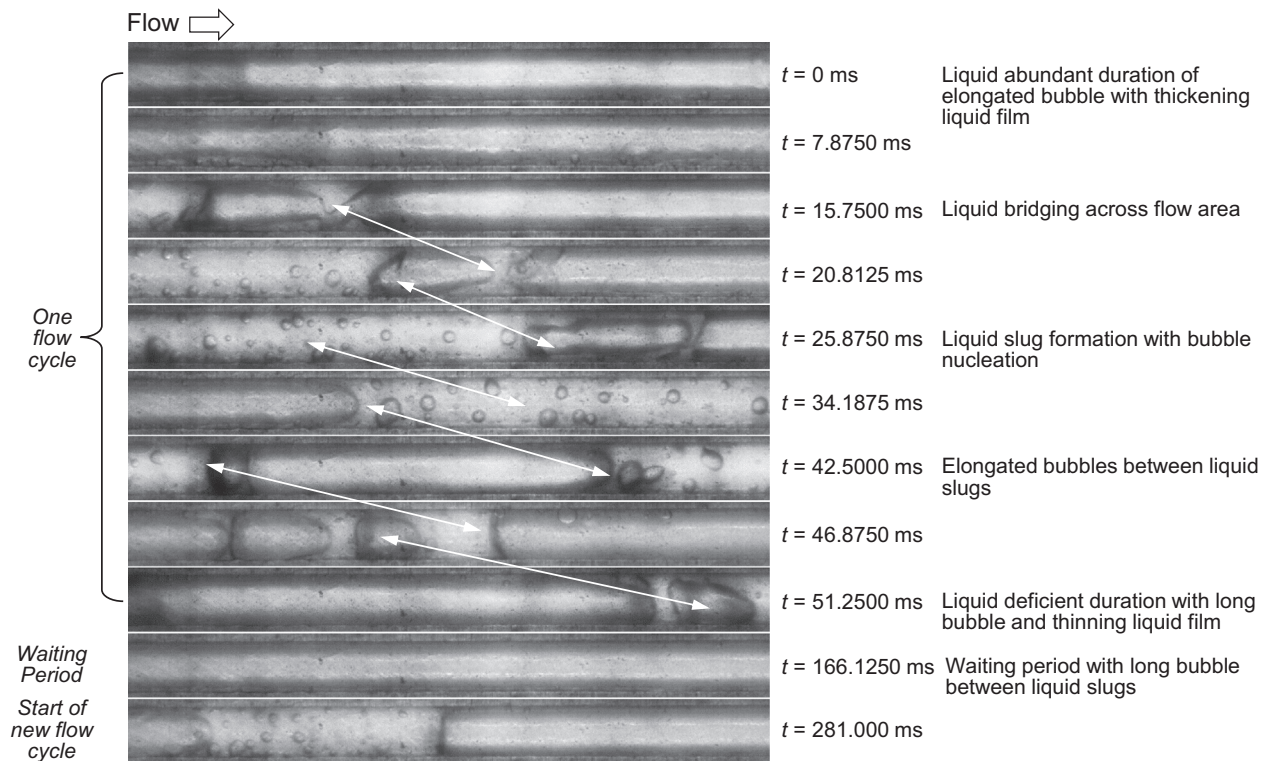
Fig. 10. Sequential images of flow boiling at axial center of crew H/X (z = 76.2 mm) for G_{crew} = 378.04 kg/m² s and q''_{crew} = 32,291.7 W/m².

waves – ripples – in the interface. Interfacial instability causes amplification of the ripples to larger waves, and increased penetration of the large waves into the vapor core causes these waves to propagate faster and coalesce with one another into yet larger amplitude waves [44]. This allows wave crests from opposite sides of the channel to merge, which is manifest with the liquid bridging depicted at t = 15.75 ms, initiating the formation of a liquid slug between long bubbles. Fed by both wave merging and surface tension pulling liquid from the liquid film, the liquid slug grows in mass as shown at t = 25.875 ms. Heat from the wall begins to nucleate bubbles within the liquid slug. Vapor content in the liquid slug increases rapidly as the bubbles grow in size and coalesce with nearby bubbles, leading to the formation of elongated bubbles as shown at t = 34.1875 ms. Captured at t = 20.8125 and 25.8750 ms is another mechanism for formation of large bubbles, which consists of vapor capture by liquid bridging between the liquid slug and the upstream long vapor bubble. Further coalescence of bubbles within the liquid slug and the intermediate large bubbles causes breakdown of the liquid slug into a combination of shorter liquid slugs and long vapor bubbles as shown at t = 42.5000 and 46.8750 ms. Vapor bubbles are elongated further, aided by liquid film evaporation, before the next flow cycle commences, with a *waiting time* between cycles of 50–200 ms. Between cycles, a long bubble with a thin liquid film is maintained between liquid slugs as shown at t = 166.1250 ms, and a new cycle is initiated with liquid slug formation as shown at t = 281.0000 ms. After several flow cycles within the liquid abundant duration, a liquid deficient duration commences, which is characterized by sequential formation and evaporation of thick and thin liquid films.

The heat transfer coefficient should increase where the film is thin, but decease considerably if film dryout is encountered during the liquid deficient duration. Dryout will occur when the film evaporation rate is too fast to maintain a liquid film before the next liquid abundant duration is initiated.

Fig. 11(a) and (b) help explain the degradation in the heat transfer coefficient at high heat fluxes and low vapor qualities for the crew H/X. Shown are dominant flow patterns corresponding to q''_{crew} = 16,146.9 and 40,364.7 W/m² on a boiling curve for G_{crew} = 340.23 kg/m² and the middle of the crew H/X, z = 76.2 mm. Indicated in Fig. 11(a) is the location of intermittent dryout, point (B), corresponding to q''_{crew} = 40,364.7 W/m², where ΔT_{crew} begins to escalate appreciably. Notice that CHF is not encountered for this condition. The cyclical flow patterns captured in Fig. 10 are encountered at low fluxes, as depicted in image sequence (A) in Fig. 11(b) corresponding to q''_{crew} = 16,146.9 W/cm². Shown are bubbles generated by nucleate boiling coalescing together to form an elongated slug flow bubble surrounded by a relatively thick film.

Heat transfer degradation is initiated by intermittent dryout caused by either (i) vapor blanket formation due to intense bubble growth and coalescence within the liquid slug, or (ii) partial dryout of the liquid film surrounding the elongated bubbles in slug flow. Both forms of intermittent dryout are encountered at point (B) in Fig. 11(a) and depicted in image sequence (B) in Fig. 11(b). Shown is bubble growth and coalescence at this relatively high heat flux inhibiting liquid access to the wall. Further heat transfer degradation is encountered by the rapid evaporation and partial dryout of the liquid film surrounding the elongated bubble. The partial dryout of the liquid film is exasperated with further increases in the heat flux.

5.3. Flow visualization results for avionics H/X

The avionics H/X features channels that are significantly longer than the crew H/X, 609.6 mm compared to 152.4 mm, which facilitates a more detailed assessment of the axial variations of the heat transfer mechanisms for the avionics H/X. Fig. 12(a) shows the variation of the two-phase heat transfer coefficient along the avionics H/X for $q''_{avionics}$ = 44,401.1 W/m² and $G_{avionics}$ =

(a)

(b)
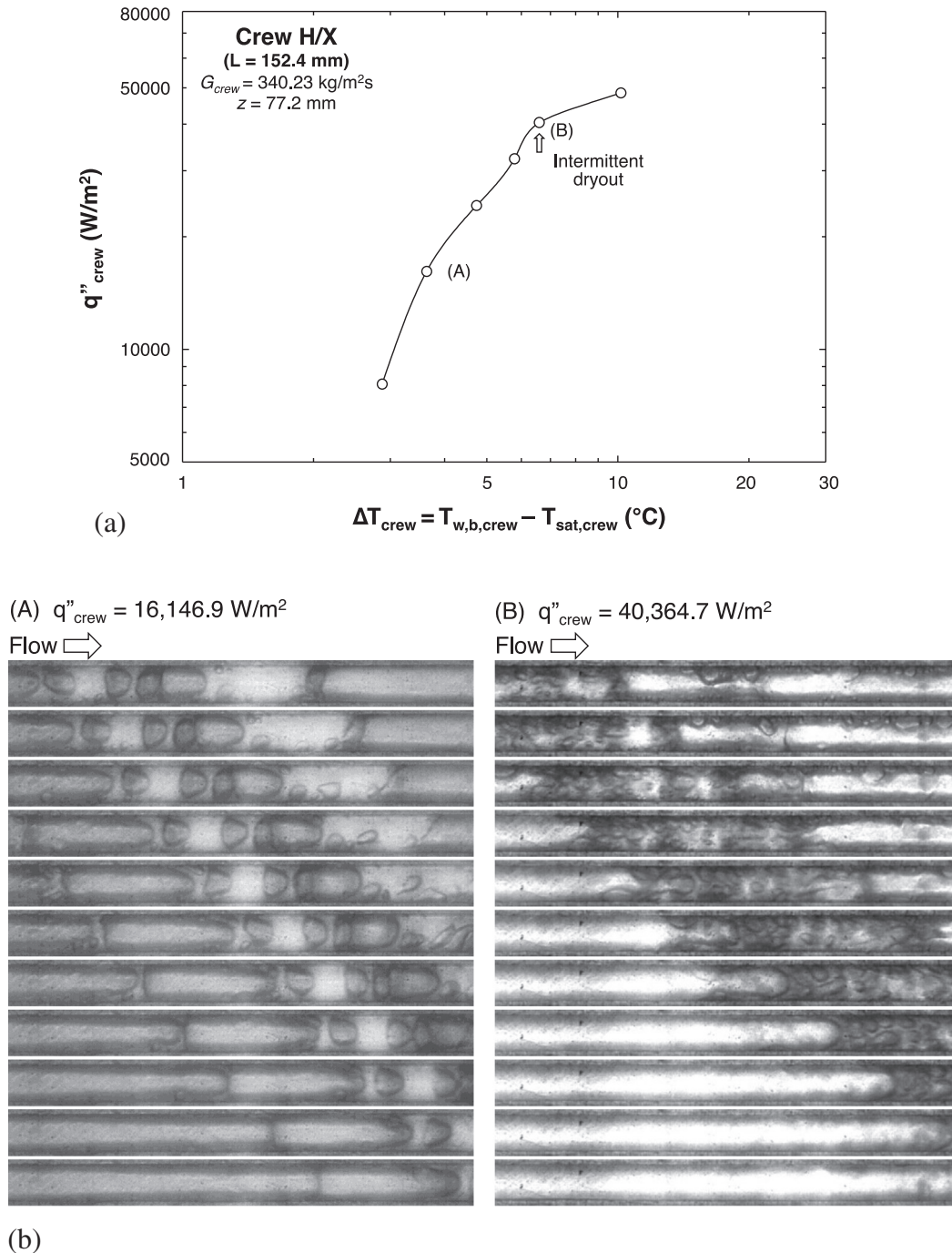
Fig. 11. (a) Boiling curve at axial centerline (z = 76.2 mm) of crew H/X for G_{crew} = 264.63 kg/m² s, and (b) image sequences of flow boiling in micro-channel at two heat fluxes. Individual images in each sequence are 1.250 ms apart.

340.23 kg/m² s, while Fig. 12(b) shows dominant heat transfer mechanisms along the micro-channel for low, mid, and high quality conditions. The dominant flow patterns and corresponding heat transfer mechanisms can be summarized as follows:

(I) *Low quality region* ($x_e < 0.36$): This region includes bubbly and slug flow patterns, with heat transfer dominated by nucleate boiling and associated with high h_{tp} values. Transition from bubbly to slug flow is the result of increased quality increasing bubble growth and coalescence. Nucleate boiling heat transfer in the slug flow regime is a combination of bubble nucleation in the liquid slugs and evaporation of the thin film surrounding the elongated bubbles as shown

in schematic (i) in Fig. 12(b). Increasing x_e within the low quality region causes elongation of the slug flow bubbles at the expense of the liquid slugs. This decreases the portion of the channel wall incurring bubble nucleation, resulting in a gradual decrease in h_{tp} as shown in Fig. 12(a), which can be exasperated by intermittent dryout either within the thin liquid film surrounding the elongated bubble or by vapor blanket formation at the wall within the liquid slug.

(II) *Mid quality region* ($0.36 < x_e < 0.50$): This region consists of annular flow, where bubble nucleation is suppressed and heat transfer dominated by convective boiling, *i.e.*, heat transfer across the film and film evaporation. The annular
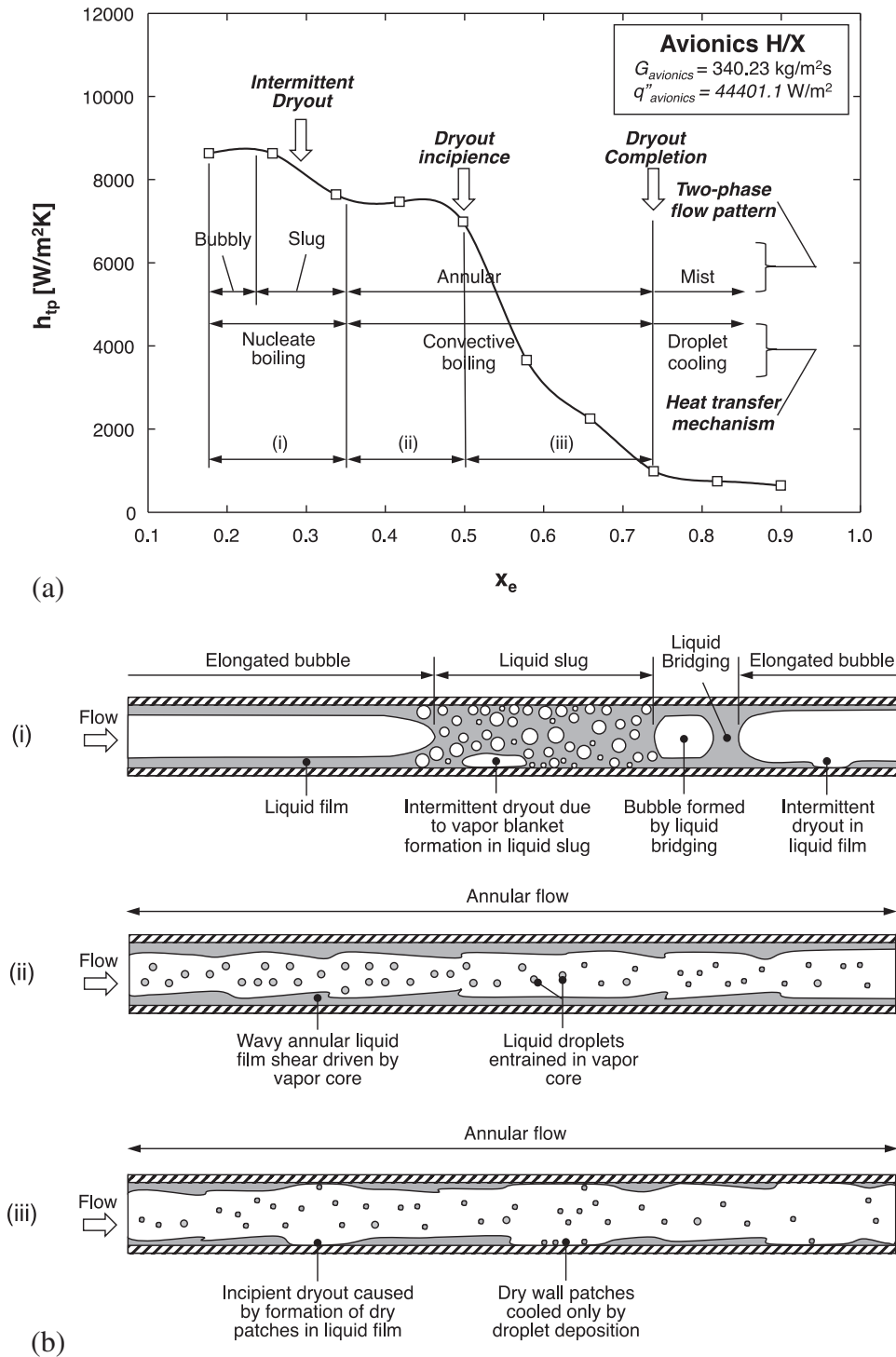
Fig. 12. (a) Variation of heat transfer coefficient with axial distance in avionics H/X at $G_{avionics}$ = 340.23 kg/m² s and $q''_{avionics}$ = 44,401.1 W/m². (b) Schematics of flow boiling for the quality ranges in (a) illustrating dominant flow patterns and heat transfer mechanisms.

liquid film is wavy and shear driven by the vapor core, which also contains entrained liquid droplets. The film thickness decreases gradually in the flow direction due to evaporation, as shown in schematic (ii) in Fig. 12(b), causing a slight increase in h_{tp}.

(III) *High quality region* (0.50 < x_e < 0.74): Like the mid quality region, this region is dominated by annular flow, with heat transfer also resulting from convective across the annular liquid film and film evaporation. However, this regime

features incipient dryout, where the thinning liquid film is locally fully evaporated, exposing the channel wall to the vapor core. As shown in schematic (iii) in Fig. 12(b), the dry-out regions increase in frequency and span along the flow direction, causing a sharp reduction in h_{tp} up to x_e = 0.74, the quality associated with dryout completion. The deposition of liquid droplets entrained in the vapor core contribute to the wall cooling in the dryout regions, which tends to move the location of dryout completion farther downstream.

Table 5
Previous saturated flow boiling heat transfer correlations.

| Authors (s)	Geometry	Fluid (s)	Quality (x_e)	Boiling regime (s)	Remarks
Chen [45]	Tube, annulus	Water, methanol, cyclohexane, pentane, heptane, benzene	$x_e = 0.01$–0.71	Convective boiling dominant	Macro-channel, annular flow, Vertical upflow/downflow
Lazarek and Black [46]	Circular tube, $D_h = 3.15$ mm	R113	$x_{e,in} = 0$ $x_{e,out} = 0.02$–0.78	Nucleate boiling dominant	Mini-channel, vertical upflow/downflow
Liu and Winterton [47]	Circular tube, annulus, $D_h = 2.95$–32.0 mm	Water, R12, R113, R114, R22, ethylene glycol	$x_e = 0.0$–0.948	Nucleate and convective boiling	Macro-channel, $G = 12.4$–8173.9 kg/m^2 s, $q_h'' = 348.9$–2.62×10^6 W/m^2, vertical/horizontal flow
Tran et al. [48]	Rectangular, $D_h = 2.40$ mm (1.70 mm $\times$ 4.06 mm), circular $D_h = 2.46$, 2.92 mm	R12, R113	$x_e < 0.94$	Nucleate boiling dominant	Mini-channel, $G = 44.0$–832.0 kg/m^2 s, $q_h'' = 3600$–$129{,}000$ W/m^2, horizontal flow
Kandlikar and Balasubramanian [49]	Circular, rectangular $D_h = 0.2$–25.0 mm	Water, R11, R12, R131B1, R22, R113, R114, R134a, R152a, R32, R132, R141b, R124, Kerosene	$x_e = 0.001$–0.987	$Re_{fo} < 100$, Nucleate boiling dominant	Micro/mini-channel, $G = 13.0$–8179.0 kg/m^2 s, $q_h'' = 0.3$–2280 kW/m^2, vertical/horizontal flow
Lee and Mudawar [23]	Rectangular $D_h = 0.349$ mm	Water, R134a	$x_{e,in} = 0.001$–0.25 $x_{e,out} = 0.49$-superheat	$x_e < 0.05$: bubbly flow and nucleate boiling dominant $x_e = 0.05$–1.0: annular flow and convective boiling dominant	Micro-channel, $G = 127$–654 kg/m^2 s, $q'' = 159{,}000$–$938{,}000$ W/m^2, horizontal flow
Bertsch [50]	Circular, rectangular, $D_h = 0.16$–2.92 mm	Water, refrigerant, FC-77, nitrogen	$x_e = 0$–1	Nucleate and convective boiling	Micro/mini-channel, $G = 20.0$–3000.0 kg/m^2 s, $q_h'' = 0.4$–115 W/cm^2, vertical/horizontal flow
Kim and Mudawar [41]	Circular, rectangular $D_h = 0.19$–6.5 mm	FC72, R11, R113, R123, R1234yf, R1234ze, R134a, R152a, R22, R236fa, R245fa, R32, R404A, R407C, R410A, R417A, CO$_2$, water	$x_e = 0$–1	Nucleate and convective boiling	$G = 19$–1608 kg/m^2 s, vertical upward/horizontal flow
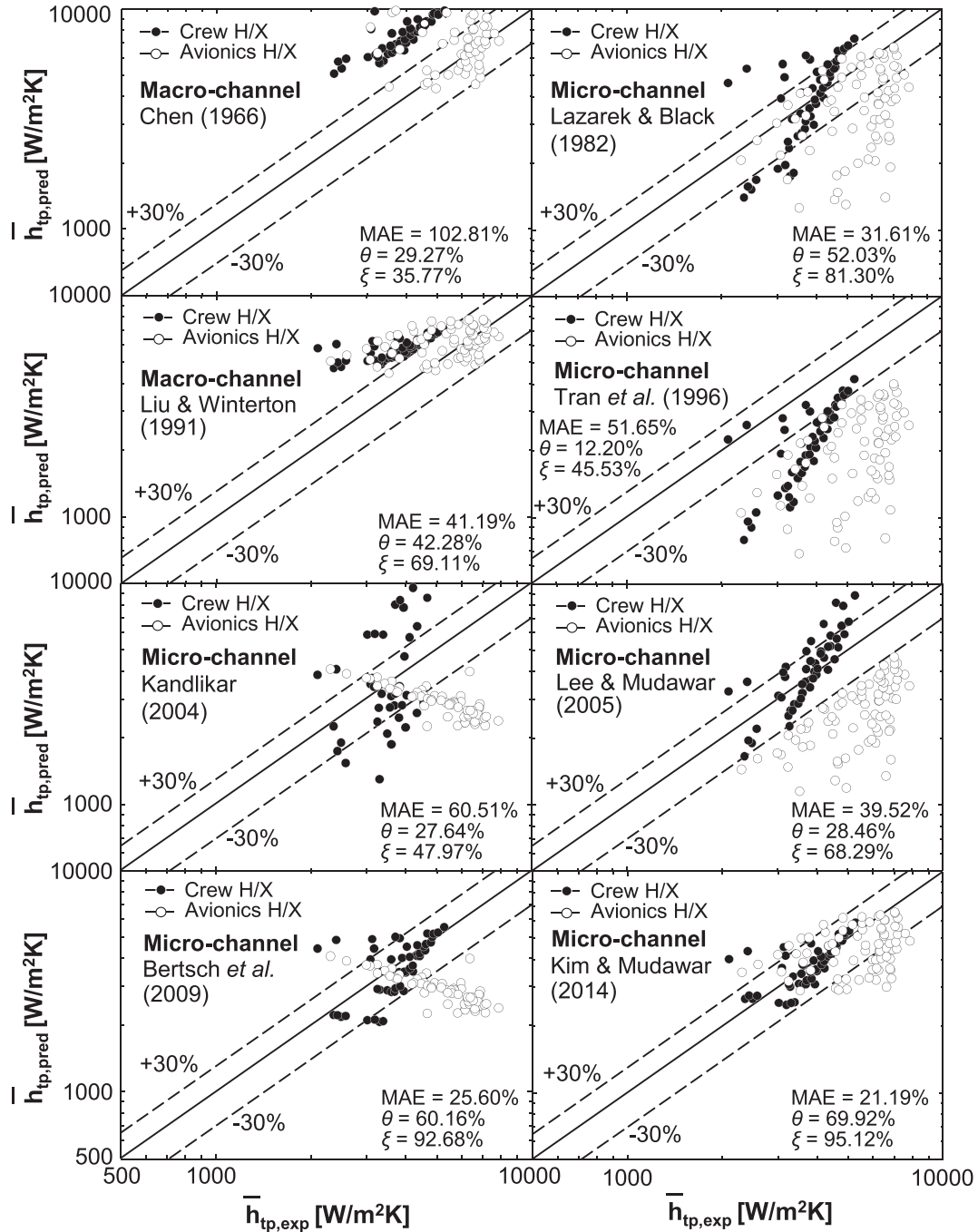
Fig. 13. Comparison of present average two-phase heat transfer coefficient data with predictions of previous correlations.

The effectiveness of the liquid deposition gradually decreases in the flow direction as the number and size of liquid droplets decreases.

For x_e > 0.74, mist flow is established, where the liquid film is fully evaporated with very mild cooling provided by remnants of the liquid droplets. Here, h_{tp} is lowest and wall temperature highest compared to the three aforementioned quality regions. It is interesting to note that the CHF commonly associated with a sharp unsteady rise in the wall temperature was never encountered for the conditions of the present study. This implies that, despite their very weak cooling effect, the liquid droplets in the mist flow regime are capable of preventing the large unsteady rise in wall temperature.

6. Assessment of prior heat transfer correlations

Several correlations have been proposed in the past for both macro and mini/micro-channels. Some of the more popular correlations, Table 5, are examined for accuracy in predicting the heat transfer coefficient data of the present study. In performing these predictions, the thermophysical properties of R134a are obtained from NIST's REPFROP 8.0 [51]. The accuracy for each correlation is evaluated using three parameters: MAE, θ and ζ. The former is the mean absolute error, which is defined as

$$MAE\,(\%) = \frac{1}{N} \sum \left[\frac{|h_{tp,pred} - h_{tp,\exp}|}{h_{tp,\exp}} \times 100 \right], \qquad (9)$$

while θ and ζ are the percentages of data points predicted within ±30% and ±50%, respectively. Most of the correlations assessed here, which are detailed in [41], were developed for circular tubes or four-sided channels subjected to a circumferentially uniform heat flux. As recommended in [41], applying the same correlations to the present three-sided heating configuration is achieved by applying the relation

$$h_{tp} = h_{tp,cor} \frac{Nu_3}{Nu_4}, \tag{10}$$

where h_{tp} and $h_{tp,cor}$ are, respectively, the two-phase heat transfer coefficients predicted for the present three-sided micro-channel configuration, and determined by a correlation for four-sided heating. In Eq. (10), Nu_3 and Nu_4 are the Nusselt numbers for thermally developed laminar flow with three-sided and four-sided heating,

$$Nu_3 = 8.235 (1 - 1.883\beta + 3.767\beta^2 - 5.814\beta^3 + 5.361\beta^4 - 2.0\beta^5), \tag{11}$$

$$\text{and} \quad Nu_4 = 8.235 (1 - 2.042\beta + 3.085\beta^2 - 2.477\beta^3 + 1.058\beta^4 - 0.186\beta^5), \tag{12}$$

respectively [41].

Fig. 13 compares average measured two-phase heat transfer coefficient data with predictions of the eight previous correlations. The measured values used in this plot are for the two-phase heat transfer coefficient averaged over the length of the respective heat exchanger,

$$\bar{h}_{tp} = \frac{1}{L} \int_0^L h_{tp}(z) \, dz. \tag{13}$$

The comparative assessment in Fig. 13 is based on 48 data points for the crew H/X and 100 data points for avionics H/X. Notice that the correlations include two that are recommended for macro-channels [45,47], and six for mini/micro-channels [23,41,46,48–50]. The two macro-channel correlations of Chen [45] and Liu and Winterton [47] are shown overpredicting the data, and the mini/micro-channel correlations of Lazarek and Black [46], Tran et al. [48], and Lee and Mudawar [23] underpredicting. The mini/micro-channel correlations that underpredict the data are based on either nucleate boiling or convective boiling relations but not both. The mini/micro-channel correlations of Kandlikar and Balasubramanian [49] and Bertsch et al. [50] fail to follow the data trend, despite the fact that they account for both nucleate boiling and convective boiling. Of the eight correlations, only the correlation by Kim and Mudawar [41] provides acceptable predictions in both accuracy and trend, evidenced by a MAE of 21.19%, with $\theta = 69.92\%$ and $\zeta = 95.12\%$ of the predictions falling within ±30% and ±50% of the data, respectively. The predictions are better for the crew H/X, with MAE = 15.01%, $\theta = 89.58\%$ and $\zeta = 95.83\%$, compared to MAE = 25.14%, $\theta = 57.33\%$ and $\zeta = 94.67\%$ for the avionics H/X.

The relative success of the Kim and Mudawar correlation can be explained by its "universal" formulation, being composed of 10,805 data points for flow boiling in mini/micro-channels amassed from 31 sources. Their database consists of 18 working fluids, hydraulic diameters of 0.19–6.5 mm, mass velocities of 19–1608 kg/m^2 s, liquid-only Reynolds numbers of 57–49,820, qualities of 0–1, and reduced pressures of 0.005–0.69. The Kim and Mudawar correlation accounts for both nucleate boiling and convective boiling, and is valid for both single channels and multi-channel heat sinks.

7. Conclusions

This study explored the two-phase heat transfer characteristics of two large micro-channel evaporators that are incorporated into an R134a vapor compression loop. The two evaporators are connected in series, with the smaller crew H/X situated upstream of the larger avionics H/X. This layout resulted in relatively low quality values in the crew H/X compared to both low and high values in the avionics H/X. With a very broad range of qualities, the study provided a systematic assessment of dominant heat transfer mechanisms, including the relative contributions of nucleate boiling and convective boiling. The relationship between these mechanisms and two-phase flow patterns, as well as vital spatial and temporal changes in interfacial features, were examined with the aid of high-speed video. Finally, the study provided an assessment of the accuracy of previous correlations in predicting the measured two-phase heat transfer coefficient for both evaporators. Key conclusions from the study can be summarized as follows:

(1) For the crew H/X, which is associated with relatively low qualities, slug flow is dominant for most operating conditions. Dominated by nucleate boiling, the two-phase heat transfer coefficient decreases monotonically with increasing quality. Heat transfer is also enhanced with increasing heat flux up to the point of intermittent dryout, following which it begins to decrease as the wall temperature escalates considerably. Intermittent dryout is shown to be the result of vapor blanket formation in the liquid slugs and/or partial dryout of the liquid film surrounding elongated bubbles. Heat transfer in the crew H/X is highly influenced by cyclical changes in interfacial behavior resulting from temporal fluctuations in the mass velocity.

(2) For the avionics H/X, which is associated with both low and high qualities, both flow pattern and heat transfer mechanism change drastically for different quality ranges. For low qualities of $x_e < 0.36$, bubbly and mostly slug flow are dominant, and heat transfer is associated mostly with nucleate boiling. For mid range of $0.36 < x_e < 0.50$, annular flow is prevalent and heat transfer is the result of convective boiling across the annular film. At $x_e = 0.5$, incipient dryout marks the point where the heat transfer coefficient begins to decrease appreciably with increasing quality because of localized dryout of the annular film. While annular flow persists in the high range of $0.50 < x_e < 0.74$, increasing quality increases the size and number of dryout regions. Complete dryout is encountered around $x_e = 0.74$, following which mist flow prevails, where the wall is mildly cooled by liquid droplets deposited from the vapor core.

(3) Eight previous correlations for two-phase heat transfer coefficient were assessed for accuracy in predicting the measured heat transfer coefficients for the crew and avionics H/Xs. They include two correlations developed for macro-channels and six for mini/micro-channels. Additionally, three of the mini/micro-channel correlations are based on either nucleate boiling or convective boiling relations but not both, while the other three account for both. Of the eight correlations, only the "universal" correlation by Kim and Mudawar [41] was shown to provide acceptable predictions in both accuracy and trend, with by a MAE of 21.19%, and 69.92% and 95.12% of the predictions falling within ±30% and ±50% of the data, respectively.

Conflict of interest

None declared.

Acknowledgements

References

[1] F.P. Chiaramonte, J.A. Joshi, Workshop on critical issues in microgravity fluids, transport, and reaction processes in advanced human support technology – final report, NASA Report TM-2004-212940, 2004.

[2] S.H. Lee, I. Mudawar, M.M. Hasan, Thermal analysis of hybrid single-phase, two-phase and heat pump thermal control system (TCS) for future spacecraft, Appl. Therm. Eng. (2016), http://dx.doi.org/10.1016/j.applthermaleng.2016.01.018. in press.

[3] M.K., Ewert, P.A. Petete, J. Dzenitis, Active thermal control systems for Lunar and Martian exploration, SAE Technical Paper 901243, 1990.

[4] I. Mudawar, Two-phase micro-channel heat sinks: theory, applications and limitations, J. Electron. Packag. – Trans. ASME 133 (2011) 041002-2.

[5] I. Mudawar, A.H. Howard, C.O. Gersey, An analytical model for near-saturated pool boiling CHF on vertical surfaces, Int. J. Heat Mass Transfer 40 (1997) 2327–2339.

[6] J.A. Shmerler, I. Mudawar, Local heat transfer coefficient in wavy free-falling turbulent liquid films undergoing uniform sensible heating, Int. J. Heat Mass Transfer 31 (1988) 67–77.

[7] J.A. Shmerler, I. Mudawar, Local evaporative heat transfer coefficient in turbulent free-falling liquid films, Int. J. Heat Mass Transfer 31 (1988) 731–742.

[8] T.H. Lyu, I. Mudawar, Statistical investigation of the relationship between interfacial waviness and sensible heat transfer to a falling liquid film, Int. J. Heat Mass Transfer 34 (1991) 1451–1464.

[9] J.C. Sturgis, I. Mudawar, Critical heat flux in a long, rectangular channel subjected to one-sided heating – II. Analysis of CHF data, Int. J. Heat Mass Transfer 42 (1999) 1849–1862.

[10] D.D. Hall, I. Mudawar, Experimental and numerical study of quenching complex-shaped metallic alloys with multiple, overlapping sprays, Int. J. Heat Mass Transfer 38 (1995) 1201–1216.

[11] M. Visaria, I. Mudawar, Theoretical and experimental study of the effects of spray inclination on two-phase spray cooling and critical heat flux, Int. J. Heat Mass Transfer 51 (2008) 2398–2410.

[12] D.D. Hall, I. Mudawar, Ultra-high critical heat flux (CHF) for subcooled water flow boiling – II. High-CHF database and design parameters, Int. J. Heat Mass Transfer 42 (1999) 1429–1456.

[13] S. Mukherjee, I. Mudawar, Smart pumpless loop for micro-channel electronic cooling using flat and enhanced surfaces, IEEE Trans.-CPMT: Compon. Packag. Technol. 26 (2003) 99–109.

[14] W. Qu, I. Mudawar, S.-Y. Lee, S.T. Wereley, Experimental and computational investigation of flow development and pressure drop in a rectangular micro-channel, J. Electron. Packag. – Trans. ASME 128 (2006) 1–9.

[15] J. Lee, I. Mudawar, Low-temperature two-phase micro-channel cooling for high-heat-flux thermal management of defense electronics, in: Proc. ITherm 2008: Int. Conf. on Thermal, Mechanics and Thermomechanical Phenomena in Electronic Systems, Orlando, FL, May 28–31, 2008, pp. 132–144.

[16] M.K. Sung, I. Mudawar, Experimental and numerical investigation of single-phase heat transfer using a hybrid jet impingement/micro-channel cooling scheme, Int. J. Heat Mass Transfer 49 (2006) 682–694.

[17] B.S. Singh, M.H. Hasan, Innovative multi-environment, multimode thermal control system, SAE Paper 2007-01-3202, 2007.

[18] S. Lin, P.A. Kew, K. Cornwell, Two-phase heat transfer to a refrigerant in a 1 mm diameter tube, Int. J. Refrig. 24 (2001) 51–56.

[19] S. In, S. Jeong, Flow boiling heat transfer characteristics of R123 and R134a in a micro-channel, Int. J. Multiphase Flow 35 (2009) 987–1000.

[20] C.B. Tibiriçá, G. Ribatski, Flow boiling heat transfer of R134a and R245fa in a 2.3 mm tube, Int. J. Heat Mass Transfer 53 (2010) 2459–2468.

[21] S. Saisorn, J. Kaew-On, S. Wongwises, Flow pattern and heat transfer characteristics of R-134a refrigerant during flow boiling in a horizontal circular mini-channel, Int. J. Heat Mass Transfer 53 (2010) 4023–4038.

[22] M. Ducoulombier, S. Colasson, J. Bonjour, P. Haberschill, Carbon dioxide flow boiling in a single microchannel – Part II: Heat transfer, Exp. Therm. Fluid Sci. 35 (2011) 597–611.

[23] J. Lee, I. Mudawar, Two-phase flow in high-heat-flux micro-channel heat sink for refrigeration cooling applications: Part II—Heat transfer characteristics, Int. J. Heat Mass Transfer 48 (2005) 941–955.

[24] B. Agostini, J.R. Thome, M. Fabbri, B. Michel, D. Calmi, U. Kloter, High heat flux flow boiling in silicon multi-microchannels – Part I: Heat transfer characteristics of refrigerant R236fa, Int. J. Heat Mass Transfer 51 (2008) 5400–5414.

[25] W. Qu, I. Mudawar, Flow boiling heat transfer in two-phase micro-channel heat sinks––I. Experimental investigation and assessment of correlation methods, Int. J. Heat Mass Transfer 46 (2003) 2755–2771.

[26] W. Qu, I. Mudawar, Flow boiling heat transfer in two-phase micro-channel heat sinks––II. Annular two-phase flow model, Int. J. Heat Mass Transfer 46 (2003) 2773–2784.

[27] J. Lee, I. Mudawar, Implementation of microchannel evaporator for high-heat-flux refrigeration cooling applications, J. Electron. Packag. – Trans. ASME 128 (2005) 30–37.

[28] K. Cornwell, P.A. Kew, Boiling in small parallel channels, in: D.P.A. Pilavachi (Ed.), Energy Efficiency in Process Technology, Springer, Netherlands, 1993, pp. 624–638.

[29] P.A. Kew, K. Cornwell, Correlations for the prediction of boiling heat transfer in small-diameter channels, Appl. Therm. Eng. 17 (1997) 705–715.

[30] A.M. Jacobi, J.R. Thome, Heat transfer model for evaporation of elongated bubble flows in microchannels, J. Heat Transfer – Trans. ASME 124 (2002) 1131–1136.

[31] J.R. Thome, V. Dupont, A.M. Jacobi, Heat transfer model for evaporation in microchannels. Part I: Presentation of the model, Int. J. Heat Mass Transfer 47 (2004) 3375–3385.

[32] J.A. Boure, A.E. Bergles, L.S. Tong, Review of two-phase flow instability, Nucl. Eng. Des. 25 (1973) 165–192.

[33] S. Kakaç, B. Bon, A review of two-phase flow dynamic instabilities in tube boiling systems, Int. J. Heat Mass Transfer 51 (2008) 399–433.

[34] W. Qu, I. Mudawar, Transport phenomena in two-phase micro-channel heat sinks, J. Electron. Packag. – Trans. ASME 126 (2004) 213–224.

[35] C. Huh, J. Kim, M.H. Kim, Flow pattern transition instability during flow boiling in a single microchannel, Int. J. Heat Mass Transfer 50 (2007) 1049–1060.

[36] G. Wang, P. Cheng, A.E. Bergles, Effects of inlet/outlet configurations on flow boiling instability in parallel microchannels, Int. J. Heat Mass Transfer 51 (2008) 2267–2281.

[37] S.J. Kline, The purposes of uncertainty analysis, J. Fluids Eng. 107 (1985) 153–160.

[38] R.J. Moffat, Describing the uncertainties in experimental results, Exp. Therm. Fluid Sci. 1 (1988) 3–17.

[39] T.L. Bergman, F.P. Incropera, A.S. Lavine, D.P. DeWitt, Fundamentals of heat and mass transfer, seventh ed., Wiley and Sons, New York, 2011.

[40] S.-M. Kim, I. Mudawar, Universal approach to predicting saturated flow boiling heat transfer in mini/micro-channels – Part I. Dryout incipience quality, Int. J. Heat Mass Transfer 64 (2013) 1226–1238.

[41] S.-M. Kim, I. Mudawar, Universal approach to predicting saturated flow boiling heat transfer in mini/micro-channels – Part II. Two-phase heat transfer coefficient, Int. J. Heat Mass Transfer 64 (2013) 1239–1256.

[42] O.C. Iloeje, A study of wall rewet and heat transfer in dispersed vertical flow Ph.D. thesis, Massachusetts Institute of Technology, Cambridge, Massachusetts, 1975.

[43] H.Y. Wu, P. Cheng, Visualization and measurements of periodic boiling in silicon microchannels, Int. J. Heat Mass Transfer 46 (2003) 2603–2614.

[44] I. Mudawar, Interfacial instabilities of air-driven liquid films, Int. Commun. Heat Mass Transfer 13 (1986) 535–543.

[45] J.C. Chen, Correlation for boiling heat transfer to saturated fluids in convective flow, Ind. Eng. Chem. Process Des. Dev. 5 (1966) 322–329.

[46] G.M. Lazarek, S.H. Black, Evaporative heat transfer, pressure drop and critical heat flux in a small vertical tube with R-113, Int. J. Heat Mass Transfer 25 (1982) 945–960.

[47] Z. Liu, R.H.S. Winterton, A general correlation for saturated and subcooled flow boiling in tubes and annuli, based on a nucleate pool boiling equation, Int. J. Heat Mass Transfer 34 (1991) 2759–2766.

[48] T.N. Tran, M.W. Wambsganss, D.M. France, Small circular- and rectangular-channel boiling with two refrigerants, Int. J. Multiphase Flow 22 (1996) 485–498.

[49] S.G. Kandlikar, P. Balasubramanian, An extension of the flow boiling correlation to transition, laminar, and deep laminar flows in minichannels and microchannels, Heat Transfer Eng. 25 (2004) 86–93.

[50] S.S. Bertsch, E.A. Groll, S.V. Garimella, A composite heat transfer correlation for saturated flow boiling in small channels, Int. J. Heat Mass Transfer 52 (2009) 2110–2118.

[51] E.W. Lemmon, M.L. Huber, M.O. McLinden, Reference fluid thermodynamic and transport properties – REFPROP Version 8.0, NIST, MD, 2007.